



**PASSIVE MULTISTATIC RADAR IMAGING
USING AN OFDM BASED SIGNAL OF
OPPORTUNITY**

THESIS

Matthew B.P. Rapson, Flight Lieutenant, Royal Australian Air Force
AFIT/GE/ENG/12-35

**DEPARTMENT OF THE AIR FORCE
AIR UNIVERSITY**

AIR FORCE INSTITUTE OF TECHNOLOGY

Wright-Patterson Air Force Base, Ohio

APPROVED FOR PUBLIC RELEASE; DISTRIBUTION UNLIMITED

The views expressed in this thesis are those of the author and do not reflect the official policy or position of the United States Air Force, Department of Defense, United States Government, the Royal Australian Air Force or the Department of Defence, Australian Government. This material is declared a work of the U.S. Government and is not subject to copyright protection in the United States.

AFIT/GE/ENG/12-35

PASSIVE MULTISTATIC RADAR IMAGING USING AN OFDM BASED
SIGNAL OF OPPORTUNITY

THESIS

Presented to the Faculty
Department of Electrical and Computer Engineering
Graduate School of Engineering and Management
Air Force Institute of Technology
Air University
Air Education and Training Command
in Partial Fulfillment of the Requirements for the
Degree of Master of Science in Electrical Engineering

Matthew B.P. Rapson, BEng
Flight Lieutenant, Royal Australian Air Force

March 2012

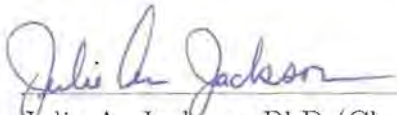
APPROVED FOR PUBLIC RELEASE; DISTRIBUTION UNLIMITED

AFIT/GE/ENG/12-35

PASSIVE MULTISTATIC RADAR IMAGING USING AN OFDM BASED
SIGNAL OF OPPORTUNITY

Matthew B.P. Rapson, BEng
Flight Lieutenant, Royal Australian Air Force

Approved:



Julie A. Jackson, PhD (Chairman)

1 Mar 2012

Date



Geoffrey A. Akers, PhD (Member)

1 Mar 2012

Date



Michael A. Temple, PhD (Member)

1 Mar 2012

Date



Alan Kerrick, PhD (Member)

2 MAR 2012

Date

Abstract

The existence of non-radar radio frequency (RF) signals in the environment possessing radar-like characteristics make them ideal candidates for use in radar applications such as synthetic aperture radar (SAR). The orthogonal frequency division multiplexing (OFDM) specific Worldwide Interoperability for Microwave Access (WiMAX) waveform is one such example.

Research at the Air Force Institute of Technology (AFIT) is focused on exploiting commercial WiMAX signals for radar applications, and an experimental OFDM radar has been developed to support research in this area. Research objectives of this work focus on achieving a proof-of-concept in using WiMAX signals within a passive, multistatic radar construct to generate simulated SAR images.

Two signal processing methods have been proposed to create phase history data. The first exploits the assumption of frequency orthogonality between two transmit signals and uses this to separate the two signals to perform parallel processing of the individual signals. The second method combines two individual reference signals to produce a single phase history in an attempt to utilize a wider signal bandwidth and therefore improve the image range resolution.

To support derivations of the signal processing methods, a software model has been created within MATLAB to simulate a SAR collection scenario. To validate the software model, experimental data collections were achieved using the OFDM radar, and the same signal processing models applied to generate experimental phase history data. Based on the software and experimental data collections, SAR images are created using a modified convolution-based filtered backprojection (FBP) algorithm.

The images generated from both experimental and simulated data were observed

to be consistent with each other, and with expectations in terms of target resolution. Coherent image addition results in improved image resolution due to the geometric and frequency diversity of the multistatic scenario compared to the individual bistatic pairs.

Acknowledgements

Firstly, I would like to thank my amazing girlfriend, who was there everyday to see me off in the morning and greet me each day upon my return home with loving arms and beautiful smile. I thank you for your support, encouragement and selflessness which continually motivate me and make all this possible. Thank you to my parents, sister and brother for their guidance and support. Even from 15000 km away, you have been there to ensure my wellbeing and keep me focused on the goal. Thanks to my family in Canada for their love and faith throughout my time in North America. I would like to extend a sincere thanks to my advisor, whose challenge and guidance has provided me with the motivation to strive for the best. Her encouragement has allowed me to realize what can be achieved on my own. Thank you also goes to my committee and other AFIT faculty for their investment and support in my research. I would like to thank the Australian Embassy staff for their generosity and time invested in ensuring a smooth and seamless transition and assistance throughout my time in the USA. Knowing the support is always there promotes the best possible learning environment. Thank you to the AFIT International Military Student Office. They have been there since day one and are always willing to provide immediate assistance when required. Finally, I would like to thank the guys in RAIL. The assistance with studies, numerous conversations on sport, family life and educating me on the American culture have made my experience in the USA and at AFIT one I will never forget. You guys provided constant positivity throughout all the ups and downs.

Matthew B.P. Rapson

Table of Contents

	Page
Abstract	iv
Acknowledgements	vi
List of Figures	ix
List of Tables	xii
I. Introduction	1
1.1 Problem Description	1
1.2 Problem Motivation	2
1.3 Research Goals and Methodology	4
1.4 Organization of Thesis	5
II. Background	7
2.1 Chapter Overview	7
2.2 Related Research	7
2.3 Important Concepts	8
2.3.1 Bistatic Radar	9
2.3.2 Passive and Multistatic Radar	10
2.3.3 Synthetic Aperture Radar	11
2.3.4 Filtered Backprojection Imaging Algorithm	16
2.3.5 Matched Filter Process	19
2.3.6 Phase Error Correction - Inverse Filtering	20
2.3.7 OFDM WiMAX Signal	22
2.4 Chapter Summary	26
III. System Description and Methodology	27
3.1 Chapter Overview	27
3.2 Signal and Geometric Model	27
3.3 Receive Signal Model	29
3.4 Signal Processing Models	30
3.4.1 Signal Separation and Parallel Processing	31
3.4.2 Combined Reference Signal	35
3.5 Assumptions	38
3.6 Software Model	39
3.6.1 User Defined Parameters	40
3.6.2 Signal Generation	41
3.6.3 Signal Processing Method Implementation	41

	Page
3.6.4 Filtered Backprojection Imaging Algorithm	43
3.6.5 Phase Error Analysis	44
3.7 Experimental Collection	46
3.7.1 Equipment System Description	46
3.7.2 Experimental Radar Configuration and Data Collection	49
3.7.3 Data Processing and Image Generation	53
3.8 Chapter Conclusion	53
IV. Results	54
4.1 Chapter Overview	54
4.2 Simulation Results	54
4.2.1 2D and 3D Simulation Validation	54
4.2.2 Simulation Image Analysis	55
4.2.3 Bandwidth and Aperture	58
4.2.4 Effective Bistatic Apertures	59
4.2.5 Combined Reference Signal Images	62
4.3 Phase Error Analysis	70
4.4 Experimental Images	73
4.4.1 Data Collect 1	74
4.4.2 Data Collect 2	76
4.4.3 Data Collect 3	78
4.4.4 Experimental Data Image Measurements	81
4.4.5 Alternate Reference Signal	82
4.4.6 Comparison to Simulated Data	82
4.5 Summary of Findings and Observations	86
4.6 Chapter Conclusion	87
V. Conclusions	88
5.1 Chapter Overview	88
5.2 Research Goals	88
5.3 Results and Contributions	88
5.4 Future Work	89
5.4.1 Research Scope	89
5.4.2 Software Model	90
5.4.3 Experimental Data Collection	90
Bibliography	91

List of Figures

Figure		Page
2.1.	Bistatic geometry	9
2.2.	Multistatic geometry example	11
2.3.	Spotlight SAR geometry	13
2.4.	SAR concept diagram	15
2.5.	Monostatic differential range	19
2.6.	OFDM time domain symbol model	23
2.7.	OFDM signal assembly	24
2.8.	WiMAX subframe assembly	24
2.9.	WiMAX signals in time domain	25
3.1.	Passive radar geometry	28
3.2.	Signal processing method 1 block diagram	31
3.3.	Filtering baseband signal - method 1	33
3.4.	Signal processing approach 2 block diagram	35
3.5.	Filtering baseband signal - method 2	37
3.6.	Range profile	43
3.7.	Phase error plot	45
3.8.	Experimental OFDM radar	46
3.9.	LPA antenna	47
3.10.	Waveform generator GUI	48
3.11.	Radar control GUI	48
3.12.	Experimental setup	50
3.13.	Experimental multistatic geometry	51

Figure		Page
3.14.	Plate target	52
4.1.	2D simulation geometry	55
4.2.	SAR images using 2D simulation	56
4.3.	3D simulation geometry	56
4.4.	Colorbar scale	57
4.5.	Single signal images	58
4.6.	Coherent combined images, method 1, 100 MHz bandwidth	60
4.7.	Collection apertures in the spatial frequency domain	60
4.8.	Coherent combined SAR images, method 1, 200 MHz bandwidth	62
4.9.	SAR images generated with negligible angular diversity	63
4.10.	Coherent combined SAR images, method 2, 100 MHz bandwidth	64
4.11.	Coherent combined image, method 2, 100 MHz bandwidth, wide aperture	64
4.12.	Carrier separation	66
4.13.	Theoretical vs measured range resolution, 100 and 200 MHz	67
4.14.	Theoretical vs measured range resolution, 20 MHz	67
4.15.	Image sidelobe plot, 100 MHz bandwidth	68
4.16.	Image sidelobe plot, 20 MHz bandwidth	68
4.17.	SAR images with linear error	71
4.18.	SAR images with quadratic error	72
4.19.	SAR images with random error	73
4.20.	SAR images from data collect 1, method 1	74
4.21.	SAR images from data collect 1, method 2	75

Figure		Page
4.22.	SAR images from data collect 2, method 1	77
4.23.	SAR images from data collect 2, method 2	78
4.24.	SAR images from data collect 3, method 1	79
4.25.	SAR images from data collect 3, method 2	80
4.26.	SAR images from data collect 4, method 1	83
4.27.	Simulated vs experimental data collect 1	84
4.28.	Simulated vs experimental data collect 2	85
4.29.	Simulated vs experimental data collect 3	85

List of Tables

Table		Page
3.1.	Experimental radar parameters	50
4.1.	Simulation parameters	57
4.2.	Signal separation and bandwidth extent (MHz)	65
4.3.	Sidelobe level (dB)	69
4.4.	Collection parameters, data collects 1-4	73
4.5.	Measured values of range resolution and sidelobe level in experimental data images	81

PASSIVE MULTISTATIC RADAR IMAGING USING AN OFDM BASED SIGNAL OF OPPORTUNITY

I. Introduction

1.1 Problem Description

The purpose of a synthetic aperture radar (SAR) system is to generate an image of the earth's surface. The resolution and quality of the image produced is dependent on numerous radar parameters, including but not limited to, the signal bandwidth, the angular extent of the signal collection, and most importantly, the timing and accurate synchronization of transmitted and received pulses.

Traditional SAR systems use signals such as the linear FM (LFM) chirp, which allows for finer range resolution through increased bandwidth within a pulse. This characteristic is generated through the technique of pulse compression. Pulse compression is achieved by using frequency or phase modulation to obtain a large bandwidth compared to that of an uncompressed pulse of the same duration [22].

There exist other radio frequency (RF) signals that inherently possess pulse compression characteristics, yet have not historically been used for SAR applications. Digital broadcast signals using orthogonal frequency division multiplexing (OFDM), such as Worldwide Interoperability for Microwave Access (WiMAX), offer properties which may be suitable for radar purposes. However, the transmission of this signal is limited to fixed stations and is outside of the radar engineer's control. This highlights the problem of using a WiMAX signal in a passive radar configuration. Passive radar introduces its own considerations specifically concerned with timing

and characteristics of the transmitted signal.

Within monostatic SAR, the synchronization or tracking of pulses is made easier given that the same platform performs both transmission and reception of the pulsed signal. The bistatic case, where the transmit and receive platforms are no longer colocated, introduces geometric considerations and additional complexity in achieving synchronization between the transmit and receive platforms. If accurate synchronization is not achieved, the image produced will be distorted and inaccurate. Distortion results from the phase errors present in the signal as a result of timing inaccuracies.

In the passive radar scenario, not only do the platform synchronization problems concerned with geometry exist, but the timing of the transmitted signal is unknown to the receiver. Therefore, the imaging problem becomes two-fold.

The feasibility of using the OFDM WiMAX signal for SAR imaging within a passive multistatic radar construct is the main goal of this research.

1.2 Problem Motivation

Bistatic radar has a long history, dating back to the beginnings of radar development. Since then, there have been periodic resurgences into bistatic radar research and applications. The research has been driven by various developments in technology and applications, mainly in the fields of missile technology, air defence systems, and satellite systems [26]. In the 1990s, a third resurgence began, and this research is still continuing at this time. This current resurgence includes research in the areas of passive bistatic radar (PBR) and bistatic SAR. This resurgence may be the result of increased computing capabilities, presence of systems which can overcome previous location and synchronization problems, such as GPS, and the increasing number of transmissions and signals within the RF environment [9].

Bistatic radar provides both advantages and disadvantages. PBR allows covert operation in collecting a received signal and offers a means to counter stealth technology [7]. Both these cases are potentially useful in the military environment. PBR systems provide the basis for multistatic systems. Multistatic radar systems, as the name suggests, are made up of numerous receivers and transmitters. These systems introduce the potential for greater amounts and diversity of information, therefore increasing resolution and accurate target reconstruction [11]. The disadvantages of such systems are an increase in complexity and signal processing relating to synchronization. The complexity ranges from managing phase synchronization between all stations or platforms, to the use of a common reference signal for accurate and consistent correlation processing. Also, there are increased requirements for signal and data processing given the increase in total information available [5]. However, development in technology such as GPS and computational power has helped to alleviate the complexity issues, and motivated research into bistatic systems which do not use their own transmitted signal. These systems exploit existing RF signals for radar functionality, using the signal as the illuminating source, and are commonly referred to as PBR, or passive coherent location (PCL) systems.

Research into PBR is driven not only by the benefits of bistatic radar mentioned above, but also by the fact that these radar systems utilize pre-existing transmitters, resulting in lower costs and elimination of frequency allocation problems. It opens up the frequency spectrum for radar systems, allowing the systems to utilize frequencies not normally allocated for radar, such as the VHF/UHF bands [7].

At the same time, there is no shortage of RF signals of opportunity present in the signal environment. Signals include amplitude modulation (AM), frequency modulation (FM), and digital television. As technology progresses, newer signals are being introduced, such as orthogonal frequency division multiplexing (OFDM)

based Worldwide Interoperability for Microwave Access (WiMAX) and long term evolution (LTE) wireless broadband technology. Based on their inherent structures, these signals may possess characteristics similar to that of a radar waveform and have the potential to be exploited for radar purposes. Current research in this area, specifically with OFDM type signals, is being conducted through the University of Rome (OFDM WiFi) and the Air Force Institute of Technology (WiMAX); both institutions have published promising experimental results [6, 13].

Despite the opportunities PBR offers various radar applications, much of the published research in this field of passive radar is focused on studies in target detection and the use of a single RF signal of opportunity, and is often shown through the use of existing hardware systems and demonstrators [3, 18, 20]. The ambiguity function properties of various signals of opportunity, including AM, FM and WiMAX, have also been studied to determine their suitability for radar functions [10, 14].

There are fewer research publications in the area of performing radar imaging with PBR systems, yet the advantages of such systems provide a range of research topics within the field. These signals of opportunity offer alternatives to the standard frequency coverage and the potential for improved bandwidth, which is directly related to the image resolution. At the same time, given the geometry of the radar transmitter, the respective receiver location can be altered to increase the aspect coverage of the scene to be imaged. PBR also offers alternatives for interferometry, an approach which combines numerous images of the same scene to add elevation resolution.

1.3 Research Goals and Methodology

The overarching goal of this research effort is to demonstrate the feasibility of performing passive radar imaging using a common commercial signal of opportunity, the

OFDM-based WiMAX signal. The research considers and accounts for the geometry defined by the passive radar configuration and uses properties of the WiMAX signal to formulate signal processing techniques. This goal is divided into three primary objectives and a single secondary objective. The three primary objectives are:

1. Investigate and develop a software algorithm to generate SAR phase history data. This is done using the multistatic radar configuration for a user defined target scene and the WiMAX signal structure.
2. Generate SAR images from the simulated phase history data, and use the images to evaluate the algorithm.
3. Conduct an experiment within the AFIT Radar Instrumentation Laboratory (RAIL) to mirror the simulation and produce simulated SAR images. This experiment utilizes the AFIT developed experimental OFDM radar.

The secondary objective is:

1. Investigate phase error effects on image formation and the application of the inverse filtering technique for phase error correction.

The result of accomplishing these goals is a working algorithm which can be used to produce SAR images from a passive OFDM signal. The target scene consists of one or more point scatterers, to ensure simplicity and provide a baseline for extended research.

This research also provides a foundation for which passive radar imaging research can be further studied at AFIT.

1.4 Organization of Thesis

This research effort is documented over five chapters. Chapter II provides the background theory and concepts investigated as part of the research. The purpose

of Chapter II is to establish notation and methods used in the research analysis to establish a foundation for the reader. The concepts of SAR imaging, bistatic/passive radar, OFDM signals, and phase correction techniques explored throughout the research effort are introduced. Chapter III defines the methodology applied throughout the research study, describing the simulation model formulation and experimental data collection. Chapter IV includes the results and analysis of applying the algorithm to generate SAR images with the OFDM-based WiMAX signals. Chapter V contains the conclusions and suggestions for future work which can be pursued from this research effort.

II. Background

2.1 Chapter Overview

The purpose of this chapter is twofold. First, it documents current research in passive radar imaging. Second, it establishes notation and explains important concepts relevant to the research, allowing the reader to understand the mathematical derivations and resulting algorithm developed and explored in this thesis.

The related research section of this chapter briefly summarizes passive radar research efforts. In particular, it focuses on research using the OFDM broadband signal. Following this, background theory and concepts are detailed to provide a baseline understanding for the reader. These include an introduction on bistatic radar and the associated geometry differences to the monostatic case. A discussion of SAR imaging and the algorithm of convolution or filtered backprojection then follows. Finally, the concept of an OFDM-based WiMAX waveform, and its potential application to radar, is introduced.

2.2 Related Research

A brief introduction to recent passive radar imaging research was provided in Section 1.2. There is limited published literature in passive SAR imaging, or even in SAR imaging with a signal of opportunity. Numerous studies of bistatic and passive radar using signals of opportunity exist [3, 6, 8, 11, 18, 20], but this has not yet extended to the application of radar imaging or SAR.

Research into Synthetic Aperture Hitchhiker Imaging, which is analogous to passive SAR imaging, has examined developing image reconstruction methods using correlation and filtered backprojection type techniques. Yarman and Yazici have extended the methods to include different configurations of transmitters and receivers,

and their derivations are presented for a generic signal. They have obtained promising numerical results based on a delta-like impulse signal, and have not focused on a specific type of signal of opportunity [27].

Current research at AFIT is specifically focusing on exploiting an OFDM-based WiMAX waveform for use in SAR. Initial studies were conducted into the feasibility of using an OFDM waveform for radar, and these are being extended to the WiMAX signal for SAR applications. Gutierrez and Jackson have published numerous papers focusing on different areas within the OFDM radar area, with results focused on OFDM range compression and imaging [13, 14]. The authors derived a range compression solution in the form of a matched filter process which was verified by a real-world experiment [12]. As part of the experiment, the authors developed an experimental OFDM radar which utilizes a MATLAB user interface. This same experimental radar is used within this research effort, and is discussed in further detail within Chapter III of this thesis.

2.3 Important Concepts

This section encompasses the background theory relevant to this thesis. It covers the concepts independently, and begins with an introduction to bistatic radar before leading into passive radar. A brief discussion of SAR imaging follows, including the processing of the received signal and the generation of phase history data. An explanation of the filtered backprojection (FBP) image processing algorithm, its implementation in MATLAB, and extension to the bistatic case is given before an introduction of the matched filter process. The inverse filtering phase error correction technique is presented prior to the section concluding with an introduction into the OFDM WiMAX signal of opportunity.

2.3.1 Bistatic Radar.

Bistatic radar is a radar system in which the transmit and receive functions are no longer performed by the same hardware (as per monostatic), but are physically or spatially separated from one another. To understand bistatic radar, it is fundamental to understand the geometry associated with such a system. Parameters of interest such as velocity and range, and therefore time delay, associated with a target are no longer dependent on a single antenna, and therefore additional aspect angles and distances are introduced when compared to the simple monostatic case.

Figure 2.1 illustrates the coordinate system of a bistatic radar [25]. R_T is defined as the distance between transmitter and target, R_R as the distance between receiver and target, θ_T and θ_R as the look angle of the transmitter and receiver with respect to North respectively, and β , the bistatic angle between the transmitter and receiver at the target. The bistatic vector, or bisector, is normal to the tangent of the isorange contour, and is defined at the angle $\frac{\beta}{2}$.

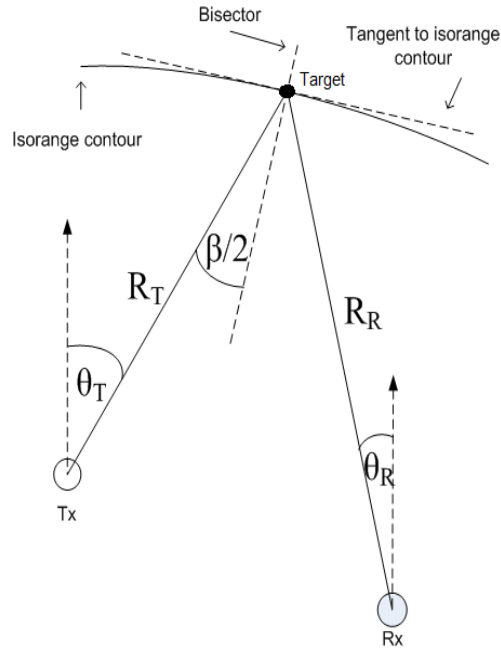


Figure 2.1. Bistatic radar coordinate system in two dimensions

Given the fact that signal propagation range is no longer simply $2R$ (as in the monostatic case, where R is the range from platform to target), the time delay τ is no longer calculated using the monostatic equation (2.1) given by

$$\tau = \frac{2R}{c}. \quad (2.1)$$

The time delay for the bistatic case, τ_{bi} is given by

$$\tau_{bi} = \frac{R_T + R_R}{c}. \quad (2.2)$$

Equation (2.2) is consistent with the indirect method of determining time delay, in which the receiver and transmitter are synchronized to a stable clock; therefore the time between pulse transmission and reception of the target return can be measured. Derivations of the respective ranges in (2.2) and how they are applied in the research effort can be found in Chapter III of this thesis.

2.3.2 Passive and Multistatic Radar.

Passive radar is a type of bistatic radar. The primary difference is that in a basic bistatic radar system the transmitter and the receiver are synchronized in some manner and the signal is known and controlled within the same radar system. In passive radar, the illuminating source is transmitted by a third party. Passive coherent location (PCL) systems exploit this third party signal, or signal of opportunity, as their own source of transmission. The advantages and drawbacks of passive systems are discussed in section 1.2. As passive systems consist of the bistatic configuration, bistatic parameters such as range can still be determined, however, the timing and parameters of the transmitted signal must first be determined.

Multistatic radar is also an extension of the bistatic radar configuration. It is

essentially any radar configuration with numerous transmitters and/or receivers; a system now consisting of multiple bistatic radar configurations. Figure 2.2 illustrates an example of a multistatic system with one receiver and three transmitters [4]. A multistatic system can become a passive system if the transmission source is a signal of opportunity which the receiver is exploiting.

For this research effort, a multistatic system of one receiver and two transmitters is assumed.

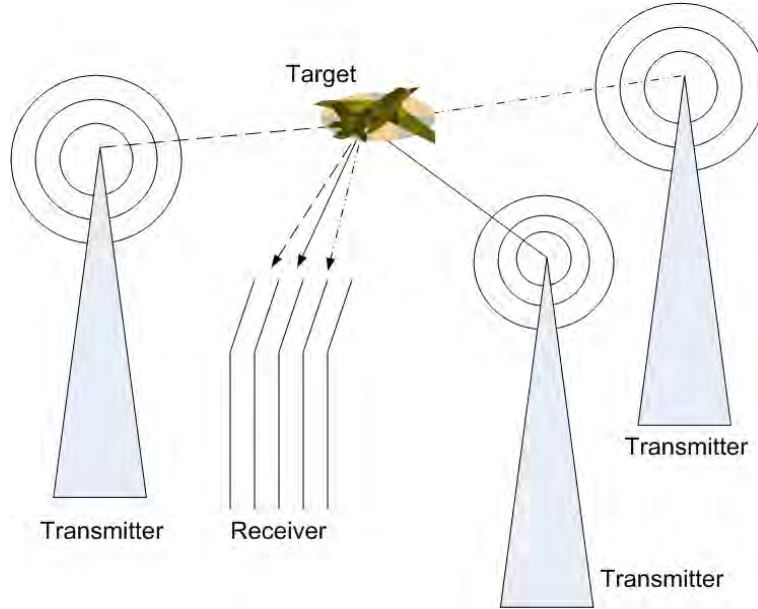


Figure 2.2. Example of multistatic geometry

2.3.3 Synthetic Aperture Radar.

Synthetic Aperture Radar (SAR) is a widely recognized remote sensing method for producing a visual representation of a target or scene of interest on the earth's surface. It has the capability to produce fine resolution, high-quality pictures, and possesses properties which overcome limitations of other remote sensing methods. SAR can be utilized in all weather conditions, day or night, and therefore is invaluable for numerous applications. SAR is commonly used for land surveying and mapping, and

is active within the military environment. Given the advantages mentioned above, SAR is employed by the military for location, identification and assessment of fixed targets [21], and is still an active research area within the radar community.

The motivation behind SAR is the improvement of cross range resolution through synthetically creating a long or wide antenna aperture. For a radar transmitting to the side of the aircraft platform, cross range resolution is the resolution obtained along the axis parallel to the flight path, whereas the standard range is in the axis perpendicular to the platform flight path. For a traditional single real-aperture radar (RAR), the cross range resolution is determined by the range to the target, the wavelength of the transmitted center frequency and the size of the antenna aperture. It can be shown that the larger the aperture, the finer the resolution in cross range. Given practical limitations, it is not possible to achieve the desired resolution with radar frequencies and standoff ranges. SAR overcomes these limitations to achieve the fine resolution required for imaging. SAR creates a “synthetic” aperture for the same wavelength and target range when compared to RAR, by effectively increasing the antenna or aperture length. The physical antenna extent is no different, but a larger antenna effective can be simulated (and accounted for in post processing) by flying along an extended flight path. Figure 2.3 illustrates the concepts of the synthetic aperture, range and cross range with respect to the aircraft platform [16].

The resolution expressions for range and cross range for a monostatic SAR image are given by

$$\rho_x = \frac{c}{2B} \quad (2.3)$$

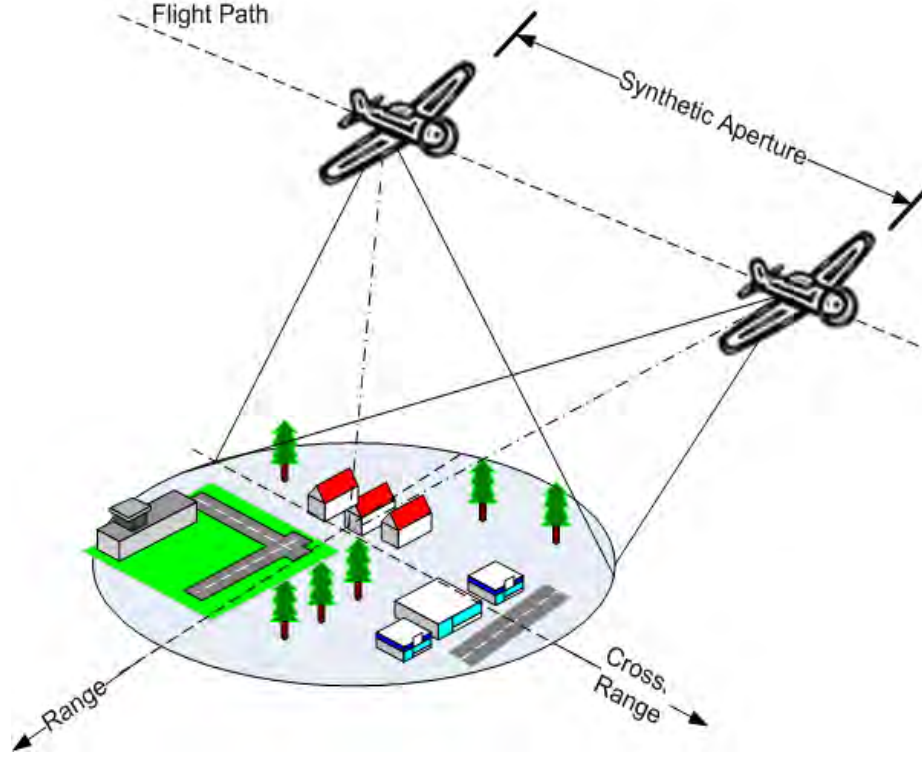


Figure 2.3. Geometry of SAR collection illustrating length of synthetic aperture, range and cross range

and

$$\rho_y = \frac{\lambda}{2\Delta\theta} \quad (2.4)$$

respectively, where c is the speed of light in m/s, B is the pulse bandwidth in Hz, λ is the pulse wavelength in meters and $\Delta\theta$ is the azimuth collection aperture in radians. For the purpose of this research effort, range is in the x direction and cross range is in the y direction.

There are different modes of SAR operation - spotlight, stripmap and scan. Spotlight mode continually slews the antenna to the same target scene on the ground as the aircraft flies along its path. Stripmap mode keeps the antenna staring broadside and flies a straight line path, illuminating a strip of the ground as the aircraft flies. Scan is a variation on stripmap, in which the strip of the scene is not parallel with the flight path [24]. In the context of this research, spotlight mode SAR is the focus.

Figure 2.3 illustrates an example of spotlight mode SAR [16].

The target of interest in SAR is the earth's surface, which can also be referred to as ground reflectivity. SAR attempts to image the ground based on the intensity of the reflectivity function, $g(u)$, where u is the range. A SAR image is an intensity representation map of the ground reflectivity function.

In simple terms, the transmitted signal convolves with the target scene reflectivity, such that the received signal is a scaled and time delayed version of the transmit signal. Given multiple scatterers within a target scene at the same range, the receive signal will consist of the integral of all the scaled, delayed signals corresponding to that range. Processing collected data from a single range will not provide an estimate across an entire target scene. That is, targets along the same range line can not be distinguished from a single pulse return. Therefore, estimates of the reflectivity function must be taken along different aspect angles relative to the scene [16].

This will provide sufficient information from which $\hat{g}(x, y)$, the estimated reflectivity function in the (x, y) plane, can be reconstructed based on each of the angles or projections. Collecting this information over different angles and generating an image from it is analogous to medical X-Ray tomography [16]. Figure 2.4 demonstrates the concepts of constant range lines and projections based on different angles, θ [16].

Let $p(x)$ represent the projection for a given angle, given by the expression

$$p(x) = \int_{-U}^U g(x, y) dx \quad (2.5)$$

where U represents the extent of ground ranges over the entire scene.

The projection slice theorem states that the one-dimensional Fourier transform of a projection function at angle θ is equal to the two-dimensional Fourier transform of $g(x, y)$ evaluated along a line/radial slice orientated at the same θ from the X-axis [15]. Therefore, storing the received signal at different angles is analogous to

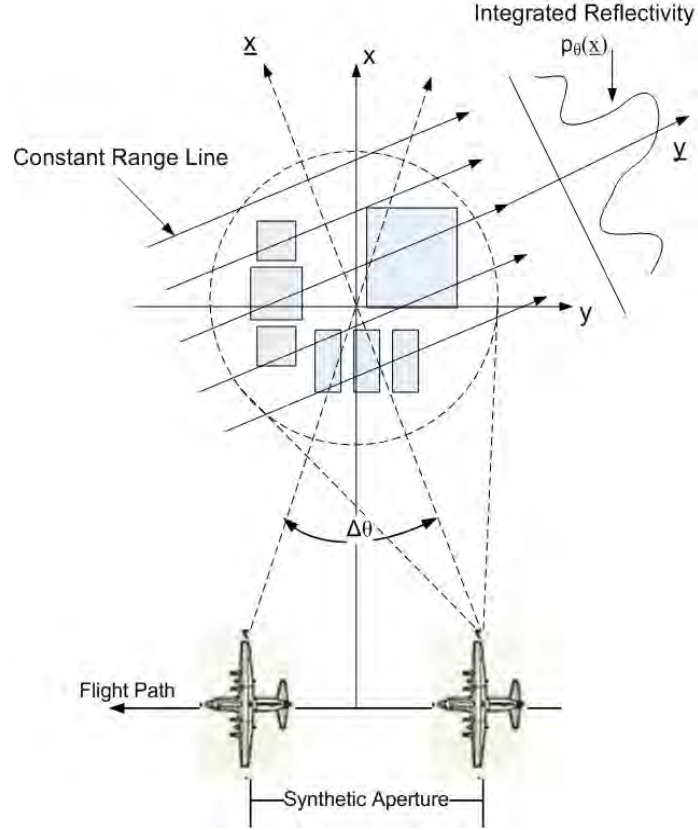


Figure 2.4. Concept of SAR imaging over multiple θ and constant range lines

performing one-dimensional Fourier transforms of the projections at each angle.

A step-by-step detailed explanation of determining the reflectivity function from a transmitted LFM signal is given in Jakowatz [16].

The concepts can be extended to the three-dimensional environment in which SAR exists. Each pulse generates values of the three-dimensional Fourier transform of $g(x, y, z)$ for a certain line segment, whose angle to the target scene is determined by ϕ and θ , the elevation and azimuth angles respectively. Over the course of the flight path, the measurements populate a line of data over each angle to produce a ribbon-like surface, or polar raster shape. The extent of the data collection surface along range is determined by the radar bandwidth. This data surface is referred to as the phase history, and the size of the data is determined by the *fast* and *slow time* samples.

The time each pulse is transmitted represents *slow time*. Each pulse return is sampled in *fast time*. For the purpose of this research, each position in the aperture represents a single transmitted pulse, which is sampled in *fast time*. Therefore, the size of the phase history is $L \times M$, where M represents the number of pulses, and L represents the number of fast time samples. The phase history data is considered to be in the spatial frequency domain. Although the data is stored in a matrix, the samples do not lie on a linear grid and are not uniformly sampled. This is a result of the collection geometry of the SAR system.

To produce an image, the phase history must be transformed into the spatial or image domain. However, simply taking a multidimensional inverse Fourier transform does not account for the non-uniformly sampled data. To perform the Fourier transform it must be assumed that the samples are uniform. There exist several algorithms to achieve this, the two most common are the polar reformatting algorithm (PFA), and the convolution or filtered backprojection. The PFA algorithm interpolates the data onto a uniformly spaced grid, however it is not the algorithm used in this research effort.

2.3.4 Filtered Backprojection Imaging Algorithm.

The convolution or filtered backprojection (FBP) algorithm constructs the image based on the properties of the Radon transform, and its origins are founded in medical tomography. The projection slice theorem mentioned in section 2.3.3 also holds for the inverse Fourier transform. The input to the filtered backprojection algorithm is the phase history data, which is effectively a collection of Fourier transforms of the projection data.

To obtain an estimate of the function $g(x, y)$, the backprojection algorithm is used as opposed to directly inverting the Radon transform. The algorithm can be divided

into four steps as follows [15]:

1. Take the 1D Fourier transform of each projection in the radial direction for each θ .
2. Apply the filter response $|\xi|$ to the transformed projection.
3. Inverse Fourier transform each filtered projection.
4. Backproject for each θ .

Step 1 is the collection of the spatial frequency domain. Step 2 is required to account for the fact that the spatial distance between points increases as you move radially away from the origin. The response of the filter at each projection is represented by $|\xi|$.

Mathematically, the reflectivity function of the image is given by [15]

$$\hat{g}(x, y) = \int_{-\theta_m/2}^{\theta_m/2} \left(\int_{\xi_1}^{\xi_2} |\xi| G(\xi, \theta) e^{j2\pi\xi(x \cos \theta + y \sin \theta)} d\xi \right) d\theta. \quad (2.6)$$

The implementation of (2.6) in MATLAB utilizes discrete samples. This is the result of the phase history in the spatial frequency domain being represented by an $L \times M$ matrix of samples. The number of fast time samples within the signal is given by L , and M is the total number of pulses or angles in the collection aperture.

To implement (2.6) in software, the expression for the convolution step for a given angle, θ_m , is given by

$$\mathbf{Q}_m = F^{-1}[(\boldsymbol{\xi} - \xi_c)\mathbf{G}_m] \quad (2.7)$$

where $\boldsymbol{\xi}$ is a vector of spatial frequencies, ξ_c is the center frequency, \mathbf{G}_m is a vector of phase history samples for a single angle, and F^{-1} is the inverse Fourier transform operator. Once \mathbf{Q}_m is computed, it is then interpolated directly onto the (x, y) grid

and phase corrected based on the relationship given by the distance to each point in the (x, y) target scene. The (x, y) grid is computed directly based on differential ranges with no computation of radial directions s . For each angle θ , \mathbf{Q}_m is interpolated to the respective ranges in the differential range matrix, which represents the differential ranges to each pixel, or range bin, in the scene. The estimated reflectivity function, $\hat{g}(x, y)$ is found by summing all phase corrected, interpolated values of \mathbf{Q}_m over all angles. The estimate of $g(x, y)$ is given by

$$\hat{g}(x, y) = \sum_{m=0}^{M-1} \hat{\mathbf{Q}}_m e^{j\alpha_c(dR)} \quad (2.8)$$

where $\hat{\mathbf{Q}}_m$ is the 1D interpolated value of \mathbf{Q}_m onto the (x, y) grid. The phase correction is given by the exponential term, where α_c is given by

$$\alpha_c = \frac{\pi f_c}{c}. \quad (2.9)$$

For the monostatic configuration, dR for a single point, (x, y, z) is given by

$$dR = 2 \left(\sqrt{(x - x_t)^2 + (y - y_t)^2 + (z - z_t)^2} - R_0 \right). \quad (2.10)$$

Equation (2.10) computes the distance between each point in the (x, y, z) plane and the distance to the scene center, given by R_0 . The first term in the expression is the radial distance between a point in the target scene and the radar platform (x_t, y_t, z_t) position at angle θ . The difference between this radial distance to some point in the target scene and the distance to the scene center, R_0 , is defined as the differential range, dR . Each range cell or pixel in the target scene will have a specific value of dR associated with it, and this value is used to phase correct the interpolated filtered projection as per (2.8). Figure 2.5 illustrates the concept of the differential

range for a target located away from scene center.

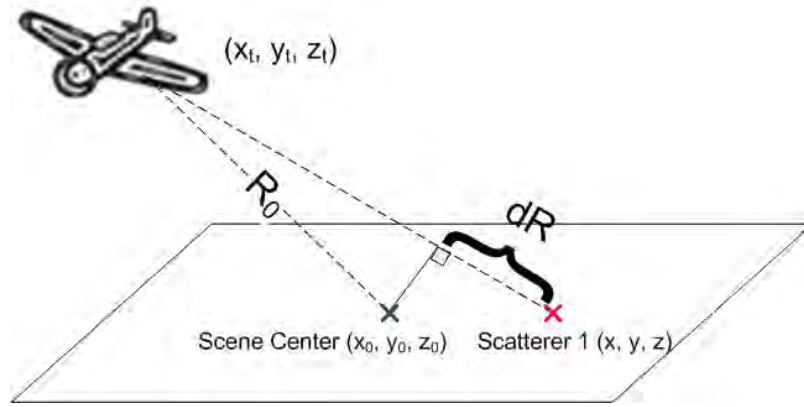


Figure 2.5. Concept of monostatic differential range, dR

However, this computation of dR does not account for the bistatic geometry of the transmitter and receiver. Therefore, the phase correction term needs to be adjusted to account for the bistatic value of dR . To account for this, the differential range term for the m th pulse is defined as

$$\begin{aligned}
 dR(m) = & x \cdot [\cos \theta_t(m) \cos \phi_t(m) + \cos \theta_r(m) \cos \phi_r(m)] \\
 & + y \cdot [\sin \theta_t(m) \cos \phi_t(m) + \sin \theta_r(m) \cos \phi_r(m)] \\
 & + z \cdot [\sin \phi_t(m) + \sin \phi_r(m)]
 \end{aligned} \tag{2.11}$$

where θ is the azimuth angle and ϕ is the elevation angle. The subscripts denote transmitter or receiver, and x , y and z are the distances within the target scene to the scene center. A derivation of this approximation is provided in Willis [26].

2.3.5 Matched Filter Process.

The matched filter process is a fundamental technique used in target detection. It is designed to maximize the signal-to-noise ratio (SNR) at a time delay corresponding to the target's range, and is desirable when there is a presence of noise in the received or measured signal. The matched filter process is used in this research as a method

to generate the phase history data, as discussed in Chapter III.

The matched filter process is fundamentally a correlation between the receive signal and the reference signal. The correlation function $g(\tau)$ is defined as

$$g(\tau) = \int_{t=0}^T s(t)s_{ref}(t - \tau)dt \quad (2.12)$$

which is a convolution in the time domain between the receive signal, $s(t)$ and the reference signal, $s_{ref}(t)$ shifted by τ [17].

The correlation above is a function of τ , and can become a function of the spatial dimension x through a transform of variables. In the monostatic case, $x = \frac{c\tau}{2}$.

When the two signals are ‘matched’, the correlation function will return a maximum value at the given delay time corresponding to τ . To implement the correlation function in an efficient manner, the Fast Fourier transform (FFT) is used. Convolution in the time domain is equivalent to multiplication in the frequency domain. Therefore, using the FFT to transform the signals to the frequency domain, $S(f)$ and $S_{ref}(f)$, allows an efficient multiplication process within a discrete environment such as MATLAB. The difference between correlation and convolution is the reversal of the reference signal in time. To achieve this time reversal in the frequency domain, the conjugate of the reference signal is used, and the correlation function is defined as

$$g(\tau) = F^{-1}[S(f)S_{ref}^*(f)]. \quad (2.13)$$

2.3.6 Phase Error Correction - Inverse Filtering.

The secondary objective of the research is to investigate the effects of phase errors on the SAR image. Phase errors are the result of inaccurate timing within the processing of the image. The demodulation timing for a bistatic radar system is given

by (2.2) relative to the scene center and is therefore proportional to accurate range determination in both the transmit and receive paths. An inaccurate demodulation time in the processing of a received pulse translates to some phase term error in the phase history data, which will result in a range error proportional to the phase error term [16].

There exist numerous techniques for applying phase correction, such as inverse filtering and autofocus. This research will address a method based on an inverse filtering method [19].

Given some corrupted phase history data, \hat{g}_ε , the goal of the inverse filtering technique is to compensate for the phase error on a single point target. Mathematically, the expression for a phase corrected phase history sample is given by

$$\hat{g}_{corr}(m, f) = \hat{g}_\varepsilon(m, f)e^{-j\hat{\gamma}(m)} \quad (2.14)$$

where \hat{g}_{corr} is the corrected phase history data for the m th pulse and f th frequency sample, and $\hat{\gamma}(m)$ is the estimated phase for the m th pulse. The estimated phase is given by

$$\begin{aligned} \hat{\gamma}(m) &= \frac{2\pi}{\lambda} r_\varepsilon(m) \\ &= 2\pi \frac{f}{c} r_\varepsilon(m) \end{aligned} \quad (2.15)$$

where r_ε is the total range error in the data collection. Within the bistatic collection, there is a need to account for both range error in both the transmit and receive ranges. Therefore, the total error is defined as

$$r_\varepsilon(m) = r_{T\varepsilon}(m) + r_{R\varepsilon}(m) \quad (2.16)$$

where $r_{T\varepsilon}(m)$ and $r_{R\varepsilon}(m)$ are the error in transmitter and receiver platform ranges respectively.

This phase error analysis technique is used to investigate the effects of the errors on the simulated SAR images. The errors defined by $r_{T\epsilon}(m)$ and $r_{R\epsilon}(m)$ will be present in the simulation as detailed in Chapter III.

2.3.7 OFDM WiMAX Signal.

The prolific amount of RF signals in the environment make them an ideal target for exploitation purposes, specifically for radar applications. As technology advances, so do the number of RF signals introduced into the signal environment. Increased interest for radar applications is demonstrated by the numerous publications analyzing the structure of various RF signals for their feasibility in PCL, some of which are discussed below.

Articles by Griffiths and Baker address the properties of different RF signals, including FM radio, analog television, cellphone network, and digital modulation signals covering both audio and video. They conclude that digital signals are more favorable for passive radar applications, but note that the target detection performance is dependent on bistatic geometry and the location of the target relative to the transmitter/receiver baseline [8, 10].

Recently, local area network (LAN) transmission and wireless networking signals have received research attention given their abundance, continual growing rate and short ranges. These signals include WiFi IEEE 802.11 and the 802.16 (WiMAX) networking standards. Gutierrez and Jackson have focused their research on the WiMAX signal, and have published works following the mathematical derivation and expressions of SAR phase history data using the OFDM signal. This derivation followed that provided in Jakowatz [16], using the OFDM signal given in (2.17).

The transmitted OFDM signal is defined by

$$s(t) = e^{j\omega_0 t} \sum_{n=-N/2}^{N/2} d_n e^{jn\Delta\omega t} \quad (2.17)$$

where ω_0 is the carrier frequency, d_n is the complex data on the n^{th} subcarrier, and $\Delta\omega$ is the subcarrier frequency spacing.

The signal bandwidth of the OFDM waveform, B is divided into N subcarriers evenly spaced in frequency, given by

$$\Delta\omega = \frac{2\pi B}{N}. \quad (2.18)$$

Each subcarrier is modulated with complex data d_n , and are combined through an inverse discrete Fourier transform (DFT) operation. Each symbol is a combination of all subcarriers, and the time domain representation of the signal is a sequence of different symbols. Figures 2.6 and 2.7 demonstrate the generation of an OFDM signal in the time domain.

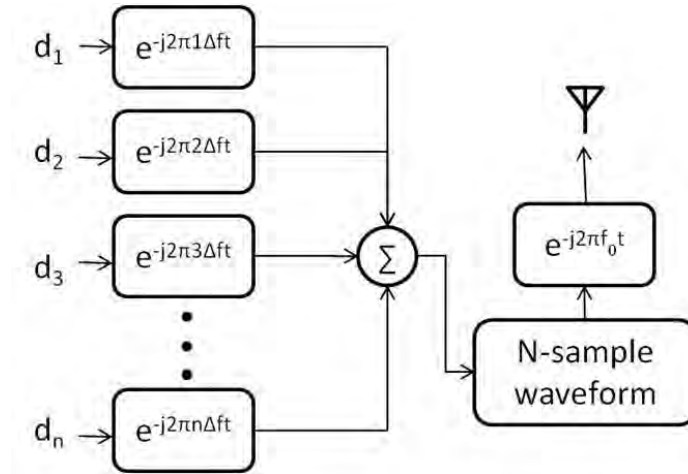


Figure 2.6. Time domain signal assembly model [13]

The WiMAX signal is a specific, standard OFDM-based signal [1]. It is widely deployed around the globe and operates in the frequency band between 2 - 11 GHz.

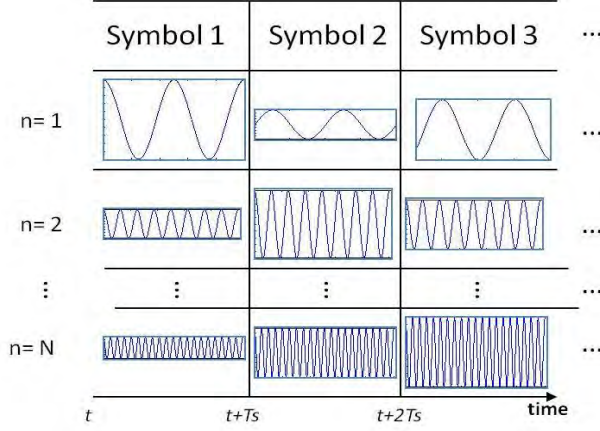


Figure 2.7. Time domain symbol assembly [13]

Of the three configurations defined by the IEEE standard, the 256-point OFDM for fixed stations is the specific signal used throughout this research.

The symbols in the time domain are transmitted via a defined frame structure, which is illustrated in Figure 2.8, and include a preamble sequence. The preamble can be made up of either one or two symbols, is dependant on the subcarriers, and always consists of the same bit sequence. It is also transmitted at 3 dB higher power levels than the data symbols. Figure 2.9 is an example of three WiMAX frames in the time domain, collected from an experimental testbed [13]. From this figure, the three frames look analogous to three radar pulses, and this is one of the reasons motivating research using the WiMAX signal for radar applications.

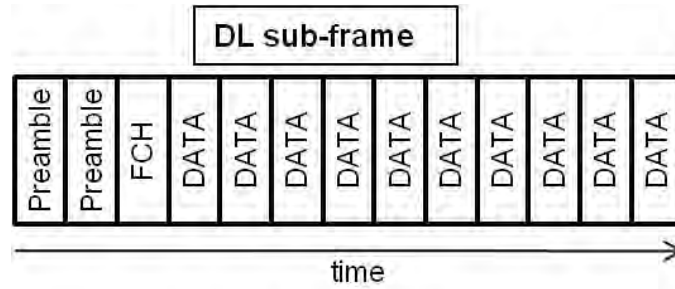


Figure 2.8. Subframe assembly of symbols [13]

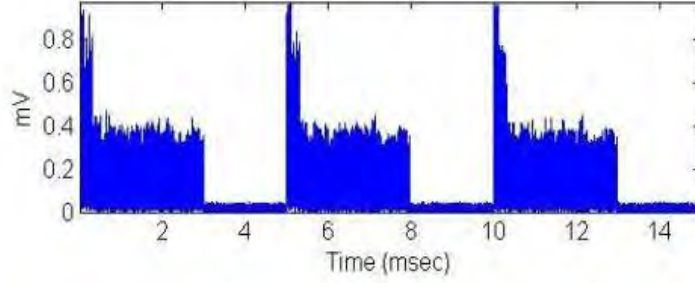


Figure 2.9. Three WiMAX frames in the time domain [13]

The IEEE standard also defines a specific sampling frequency based on the bandwidth of the signal, B . The sampling frequency is defined as

$$f_s = 8000 \left\lceil \frac{nB}{8000} \right\rceil \quad (2.19)$$

where n is a sampling factor greater than 1 and whose value is determined by the channel bandwidth. There are five possible values of n : $n=8/7$, $86/75$, $144/125$, $316/275$, $57/50$. Each corresponds to channel bandwidths that are multiples of certain frequencies, as defined by the standard [1]. For the purposes of this research, the bandwidth of the signal is always slightly greater than that listed, based on the factor n . For example, a signal with a bandwidth of 100 MHz, with a sample factor of $144/125$, will actually have a bandwidth of 115.2 MHz.

This is worth noting within the radar construct as an increase in signal bandwidth leads to a finer range resolution, as defined by (2.3).

The graphics presented in Section 2.3.7 are re-used with permission from the authors of [13].

2.4 Chapter Summary

This chapter introduced the current and previous research into passive radar imaging before providing the general theory into each of the technical concepts fundamental to this thesis. Bistatic radar involves added geometric complexities over the monostatic configuration. SAR imaging is the method of processing received radar signals to produce an image of the earth's surface, exploiting Fourier transform properties. The filtered backprojection algorithm and the bistatic modification was introduced as it is the imaging algorithm used to produce the images for this research. A brief summary of the OFDM, and specifically the WiMAX signal, was provided, including its mathematical expression which is relevant in chapter III. The next chapter will link all of this background theory into the research effort related to the mathematical derivation, software simulation and laboratory experiment.

III. System Description and Methodology

3.1 Chapter Overview

To determine the feasibility of generating SAR images using WiMAX signals, a logical and sequential effort was founded. This chapter details the steps and procedures formulating the effort, starting with the mathematical derivations, through to implementing the proposed models in software, and processing measured experimental data. An explanation of the software simulation steps is provided before an overview of the experimental radar hardware and data collection method is given.

3.2 Signal and Geometric Model

The research problem is founded on the multistatic radar construct, which is a combination of different bistatic radar configurations. Each combination of a transmitter and receiver is referred to as a bistatic pair. For example, transmitter 1 with a single receiver is referred to as bistatic pair 1. Each bistatic pair will have its own parameters, such as amplitude and time delay, associated with a target.

A representation of the passive, multistatic radar geometry is illustrated in Figure 3.1. Each of the transmitter platforms are located at a stationary location in cartesian coordinates given by (x_{tp}, y_{tp}, z_{tp}) , where the subscript represents the p th transmitter. The receiver platform will exist at a location (x_r, y_r, z_r) over the given flight path at any given point in time. The scatterer is stationary at some location in the (x, y, z) plane.

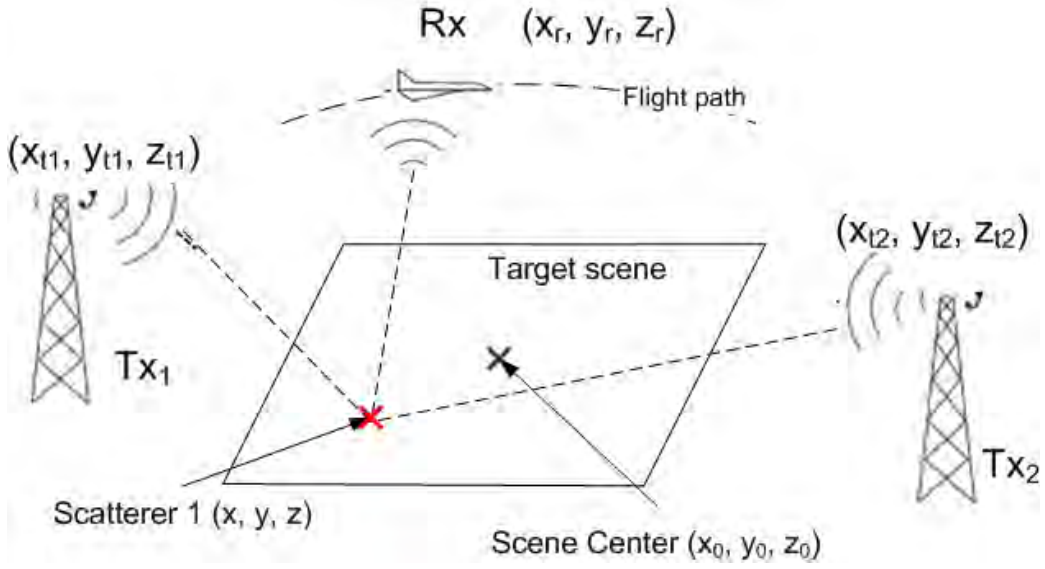


Figure 3.1. Passive radar geometry

The time delay associated with a scatterer is a function of transmitter and receiver range as given by (2.2). The time delay for the p th pair is given by

$$\tau_p = \frac{R_p}{c} \quad (3.1)$$

where

$$R_p = \sqrt{(x_{tp} - x)^2 + (y_{tp} - y)^2 + (z_{tp} - z)^2} + \sqrt{(x_r - x)^2 + (y_r - y)^2 + (z_r - z)^2} \quad (3.2)$$

is the total transmitter-target-receiver path length. Each scatterer, located at an individual (x, y, z) , will produce a different delay and reflectivity function, so the received signal will actually be a summation of each of these scatterers from each different signal.

Disregarding specific signal parameters or reflectivity functions, the generic receive signal at a given point in time, t , is composed of the summation of P transmitters. For a configuration of P transmitters and one receiver, the receive signal is given by [2]

$$r(t) = \sum_{p=1}^P \vartheta s_p(t - \tau_p) + w \quad (3.3)$$

where ϑ is the complex reflectivity and w is white Gaussian noise. The received signal is the combination of the time delayed version of each of the transmitted signals - each signal is delayed according to their respective ranges - and mixed with the reflectivity function of the ground patch.

3.3 Receive Signal Model

Recall the transmit signal for the OFDM waveform is given by

$$s(t) = e^{j\omega_0 t} \sum_{n=-N/2}^{N/2} d_n e^{jn\Delta\omega t}. \quad (3.4)$$

Following the same derivation given in [16], it can be shown that the receive signal for a single OFDM transmitter is [13]

$$r(t) = A_1 \int_{-u_1}^{u_1} g(u) e^{j(\omega_0(t-\tau_0-\tau(u)))} \sum_{n=-N/2}^{N/2} d_n e^{jn\Delta\omega(t-\tau_0-\tau(u))} du \quad (3.5)$$

where $\tau(u)$ and $g(u)$ are the time delay and reflectivity function for scatterers at range u , A_1 is the amplitude, and τ_0 is the time delay associated with the scene center. The integral represents the combination of all returns from the ranges over the extent of u_1 .

The parameter τ_0 is defined as

$$\tau_0 = \frac{R_0}{c} \quad (3.6)$$

where

$$R_0 = \sqrt{(x_t - x_0)^2 + (y_t - y_0)^2 + (z_t - z_0)^2} + \sqrt{(x_r - x_0)^2 + (y_r - y_0)^2 + (z_r - z_0)^2}. \quad (3.7)$$

Combining equations (3.3) and (3.5), the equation for a receive signal in the presence of P OFDM transmitters is defined as

$$r(t) = \sum_{p=1}^P \left(A_p \int_{-u_1}^{u_1} g(u) e^{j(\omega_{0p}(t-\tau_{0p}-\tau_p(u)))} \sum_{n=-N/2}^{N/2} d_n e^{jn\Delta\omega(t-\tau_{0p}-\tau_p(u))} du \right). \quad (3.8)$$

For SAR, the next step in the signal processing of a receive signal is the deramp process. This process involves mixing the receive signal with $e^{(-j\omega_{0p}(t-\tau_{0p}))}$, where p represents a given carrier, and filtering the signal to remove the higher frequency components resulting from the mixing process [16]. As the receive signal consists of multiple carrier frequencies and time delays, a problem arises as to which carrier and time delay to deramp the receive signal with.

3.4 Signal Processing Models

This section details two proposed models for processing the receive signal in the presence of two WiMAX transmitters. A flow diagram of each model is presented, the mathematical derivation behind each model is detailed, and figures of the signals in the frequency domain provide a graphical representation of the respective approaches.

3.4.1 Signal Separation and Parallel Processing.

The first approach to addressing the complexity of multiple carriers in the receive signal is to separate the two signals. Figure 3.2 illustrates this process. This method exploits the orthogonality between the carrier frequencies of signals 1 and 2.

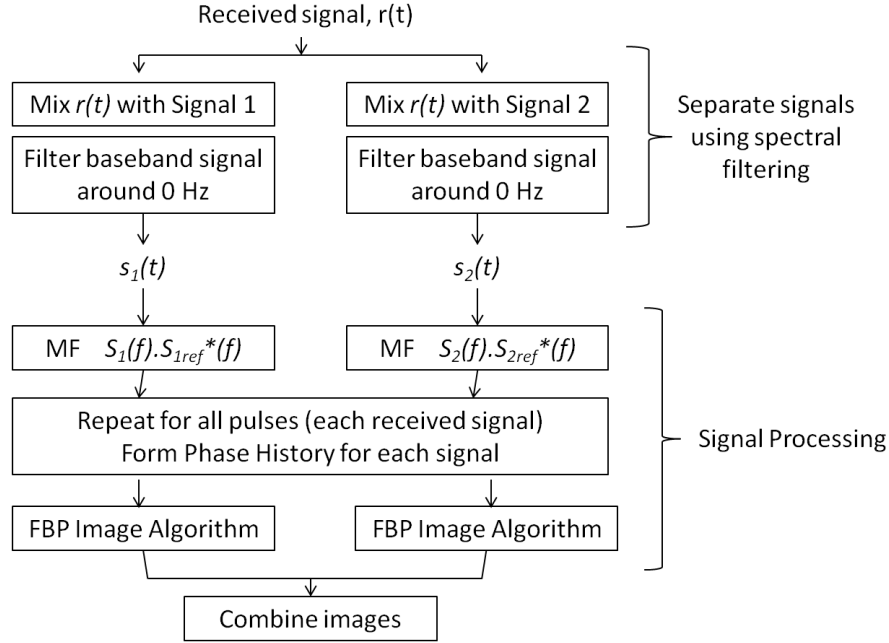


Figure 3.2. Block diagram of parallel processing approach

The receive signal $r(t)$ is first deramped with the exponential for carrier 1, ω_{01} and delayed by τ_{01} . To achieve this step, the receive signal given by (3.8) for $P=2$ is mixed with the in-phase, $\mathbf{Re}\{e^{-j\omega_{01}(t-\tau_{01})}\}$ and quadrature, $-\mathbf{Im}\{e^{-j\omega_{01}(t-\tau_{01})}\}$, (I&Q) channels. This deramp step is mathematically defined by mixing the receive signal with $\cos(\omega_{01}(t - \tau_{01}))$ (real) and $-\sin(\omega_{01}(t - \tau_{01}))$ (imaginary).

The result of this deramp process leads to the expression

$$\begin{aligned}
\tilde{r}_1(t) = & \frac{A_1}{2} \int_{-u_1}^{u_1} g(u) e^{-j(\omega_{01}\tau_1(u))} \sum_{n=-N/2}^{N/2} d_n e^{jn\Delta\omega(t-\tau_{01}-\tau_1(u))} du \\
& + \frac{A_1}{2} \int_{-u_1}^{u_1} g(u) e^{j(2\omega_{01}t-2\omega_{01}\tau_{01}-\omega_{01}\tau_1(u))} \sum_{n=-N/2}^{N/2} d_n e^{jn\Delta\omega(t-\tau_{01}-\tau_1(u))} du \\
& + \frac{A_2}{2} \int_{-u_1}^{u_1} g(u) e^{j((\omega_{02}+\omega_{01})t-\omega_{02}\tau_{02}-\omega_{02}\tau_2(u)-\omega_{01}\tau_{01})} \sum_{n=-N/2}^{N/2} d_n e^{jn\Delta\omega(t-\tau_{02}-\tau_2(u))} du \\
& + \frac{A_2}{2} \int_{-u_1}^{u_1} g(u) e^{j((\omega_{02}-\omega_{01})t-\omega_{02}\tau_{02}-\omega_{02}\tau_2(u)+\omega_{01}\tau_{01})} \sum_{n=-N/2}^{N/2} d_n e^{jn\Delta\omega(t-\tau_{02}-\tau_2(u))} du.
\end{aligned} \tag{3.9}$$

The four terms of (3.9) are each centered about the frequency defined by their first exponential. Therefore, it is possible to filter out the higher frequency components defined by the three latter terms in the expression. Using a filter to remove these components leads to the baseband signal defined by the single term

$$s_1(t) = \frac{A_1}{2} \int_{-u_1}^{u_1} g(u) e^{-j(\omega_{01}\tau_1(u))} \sum_{n=-N/2}^{N/2} d_n e^{jn\Delta\omega(t-\tau_{01}-\tau_1(u))} du. \tag{3.10}$$

If the receive signal $r(t)$ is deramped with the exponential for carrier 2, ω_{02} and delayed by τ_{02} , the same expression in (3.9) is derived, except the subscripts for two signals are reversed. Applying the same filtering concept, the resulting single term baseband signal from processing with the second signal is given by

$$s_2(t) = \frac{A_2}{2} \int_{-u_1}^{u_1} g(u) e^{-j(\omega_{02}\tau_2(u))} \sum_{n=-N/2}^{N/2} d_n e^{jn\Delta\omega(t-\tau_{02}-\tau_2(u))} du. \tag{3.11}$$

In (3.9), (3.10) and (3.11), the subscripts correspond to the parameters associated with the respective transmit signals and bistatic pair.

If the radar configuration is simplified by assuming the transmitter 2 signal and geometric parameters are the same as transmitter 1, then (3.9) reduces down the monostatic case, with the amplitude term now a factor-of-two greater. This result is expected, as it represents the case of two transmitters, or a signal with twice the power. Therefore expect twice the signal to noise ratio (SNR).

Using this deramp and filtering approach, it is possible to separate the two receive signals into signal 1 and signal 2. This process can be extended from 2 up to P orthogonal transmitters. An example of the baseband and filtered signal is shown in Figure 3.3.

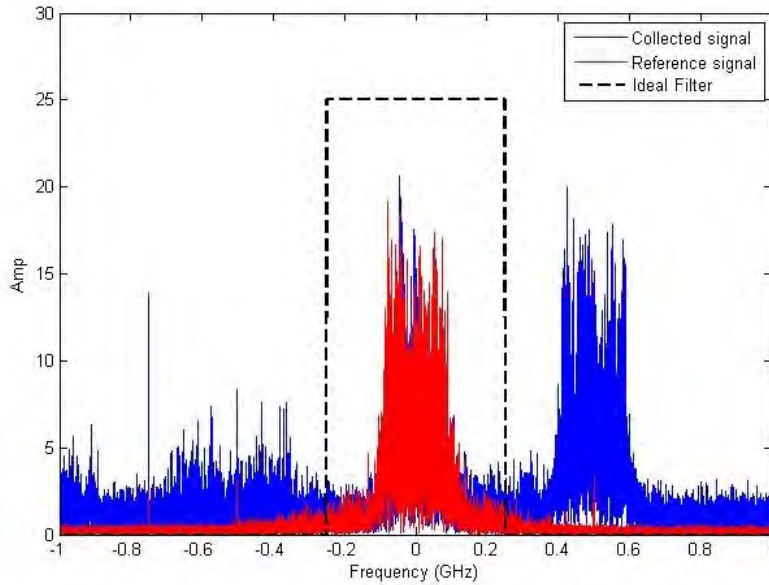


Figure 3.3. Filtering of baseband signal to isolate signal 1

The next step in the parallel processing method is to produce phase histories, or spatial frequency data, for each of the signals. This is achieved through a matched filter process. The matched filtering process used to generate phase histories was developed by Gutierrez [12]. Gutierrez showed that the phase history can be generated by matching the return signal (or receive signal) with the complex modulation data in the frequency domain. Given that fact that the WiMAX preamble data is always

the same, but modulated by a different carrier, the preamble can be defined as the complex modulation data.

Following the range profiling approach by Soumekh [23], the matched filter approach is represented by

$$\mathbf{G}_m = S_p(f)S_{pref}^*(f) \quad (3.12)$$

where \mathbf{G}_m is the phase history data vector for a given pulse m , $S_p(f)$ is the separated p th signal in the frequency domain, and $S_{pref}^*(f)$ is the baseband reference signal in the frequency domain. The reference signal is the WiMAX preamble data, modulated onto the same carrier frequency and time-delayed by the range to the scene center as the signal of interest.

The processing of the signals occurs simultaneously, therefore producing two signal processing streams, one for each transmitted signal. The result of this processing approach is an $L \times M$ matrix of phase history data for each signal stream, where L is the number of fast time samples within the signal S_p and M is the total number of pulses or angles in the collection aperture.

3.4.2 Combined Reference Signal.

The first signal processing method mixed the receive signal using individual signal characteristics to separate and produce two signal processing streams. The second method does not attempt to achieve separation, but processes the receive signal as one using a combination of the two reference signals. This approach in processing the received signal given by (3.8) is to baseband the entire receive signal by deramping with the average of the two carrier frequencies.

The average frequency, ω_{mid} , is defined by

$$\omega_{mid} = \frac{\omega_1 + \omega_2}{2} \quad (3.13)$$

Figure 3.4 illustrates the combined reference signal approach.

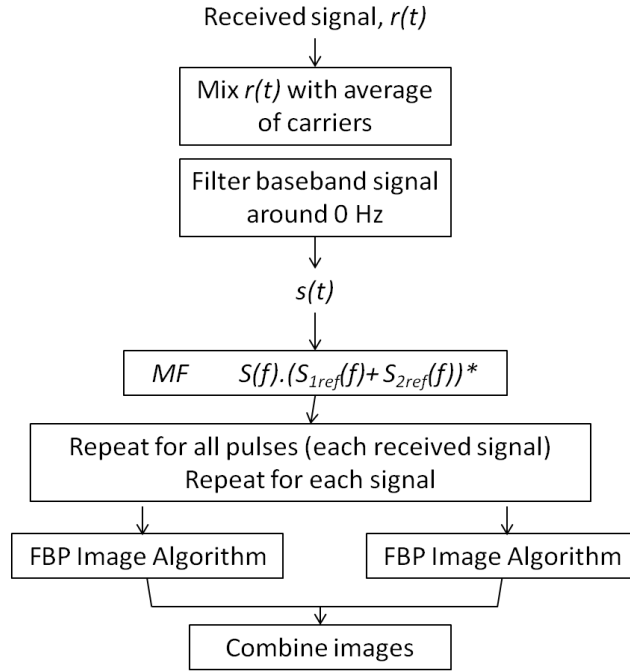


Figure 3.4. Block diagram of combined reference signal approach

The receive signal, $r(t)$ is first deramped with the exponential $e^{(-j\omega_{mid}(t-\tau_0))}$, defined by ω_{mid} and delayed by τ_0 , the time delay to the scene center. For simplicity, it is assumed that the two transmitters are the same range to the scene center for this method. The result of this deramp process leads to the expression

$$\begin{aligned}
\tilde{r}_2(t) = & \frac{A_1}{2} \int_{-u_1}^{u_1} g(u) e^{j((\omega_{01}+\omega_{mid})(t-\tau_0)-\omega_{01}\tau_1(u))} \sum_{n=-N/2}^{N/2} d_n e^{jn\Delta\omega(t-\tau_{01}-\tau_1(u))} du \\
& + \frac{A_1}{2} \int_{-u_1}^{u_1} g(u) e^{j((\omega_{01}-\omega_{mid})(t-\tau_0)-\omega_{01}\tau_1(u))} \sum_{n=-N/2}^{N/2} d_n e^{jn\Delta\omega(t-\tau_{01}-\tau_1(u))} du \\
& + \frac{A_2}{2} \int_{-u_1}^{u_1} g(u) e^{j((\omega_{02}+\omega_{mid})(t-\tau_0)-\omega_{02}\tau_2(u))} \sum_{n=-N/2}^{N/2} d_n e^{jn\Delta\omega(t-\tau_{02}-\tau_2(u))} du \\
& + \frac{A_2}{2} \int_{-u_1}^{u_1} g(u) e^{j((\omega_{02}-\omega_{mid})(t-\tau_0)-\omega_{02}\tau_2(u))} \sum_{n=-N/2}^{N/2} d_n e^{jn\Delta\omega(t-\tau_{02}-\tau_2(u))} du .
\end{aligned} \tag{3.14}$$

The four terms of (3.14) are each centered about the frequency defined by their first exponential. Therefore, it is possible to filter out the higher frequency components defined by two summation terms (terms 1 and 3) in the expression. Using a filter to remove these components leads to the baseband signal

$$\begin{aligned}
s(t) = & \frac{A_1}{2} \int_{-u_1}^{u_1} g(u) e^{j((\omega_{01}-\omega_{mid})(t-\tau_0)-\omega_{01}\tau_1(u))} \sum_{n=-N/2}^{N/2} d_n e^{jn\Delta\omega(t-\tau_{01}-\tau_1(u))} du \\
& + \frac{A_2}{2} \int_{-u_1}^{u_1} g(u) e^{j((\omega_{02}-\omega_{mid})(t-\tau_0)-\omega_{02}\tau_2(u))} \sum_{n=-N/2}^{N/2} d_n e^{jn\Delta\omega(t-\tau_{02}-\tau_2(u))} du .
\end{aligned} \tag{3.15}$$

The bandwidth of the baseband signal is no longer limited by the bandwidth of a single signal, but determined by the carrier frequency separation of the two signals.

The extent of the bandwidth is now given by the expression

$$\left(\omega_{01} - \frac{B_1}{2}\right) - \omega_{mid} \leq B \leq \left(\omega_{02} + \frac{B_2}{2}\right) - \omega_{mid} . \quad (3.16)$$

Figure 3.5 provides an example of the baseband and filtered signal. Notice the center of the two signals is at 0 Hz. In this example, the two carrier frequencies are offset in frequency by 500 MHz, and the two signals are of 200 MHz bandwidth. Using (3.16) and accounting for the increased WiMAX sampling factor, the total bandwidth is found to be approx 735 MHz.

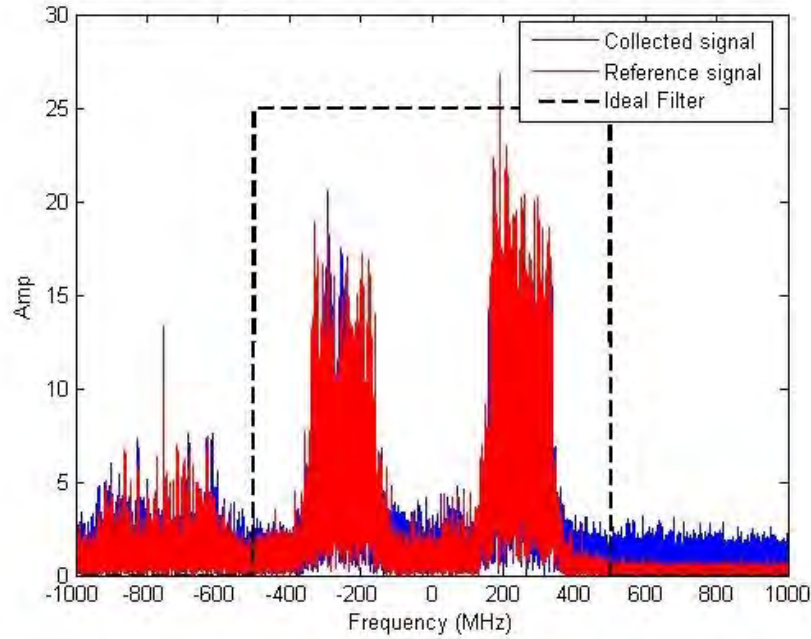


Figure 3.5. Filtering of receive signal at baseband

The next step in this processing method is to produce phase histories, or spatial frequency data, for the signal. This is achieved through a similar matched filter process as the previous method. As the receive signal now contains both of the signals at baseband, the reference signal needs to consist of both the carrier frequencies. The

matched filter process under this method generates the phase history given by

$$\mathbf{G}_m = S(f)[S_{1ref}(f) + S_{2ref}(f)]^* \quad (3.17)$$

where $S(f)$ is the deramped receive signal in the frequency domain. The reference signal for this second approach is a combination of the two deramped reference signals in the frequency domain. The result of this processing approach is an $L \times M$ matrix of phase history data, where L is the number of fast time samples within the signal S and M is the total number of pulses or angles in the collection aperture.

The final step of the signal processing for both methods is storing all the relevant radar geometric and transmitted signal parameters. A data structure is created for each signal, and includes all the parameters as well as the phase history matrix and frequency vectors.

3.5 Assumptions

Throughout this research, numerous assumptions were made to scope a complex problem to the proof of concept level. This section will list each of the assumptions used in the simulations and the lab experiment. Some assumptions have already been mentioned, where relevant, within the document. The assumptions are:

- The target scene consists of a single point scatterer, so the reflectivity function is a delta function in the spatial domain.
- The receive platform flies a constant level flight path, with no position variations in the z plane. During the phase error analysis, this assumption may be disregarded.
- The multistatic configuration consists of two fixed transmitters and one receiver.

- A single pulse is transmitted by each platform for each angle within the collection aperture.
- The receiver platform movement is negligible during pulse reception.
- There is negligible Doppler.
- The geometry of the configuration is known. That is, the ranges and angles of all the platforms to the scene center is known.
- The data transmitted in the preamble, and the signal parameters such as carrier frequency ω and bandwidth B , are known.
- Both transmit signals have the same pulse repetition frequency (PRF), and are transmitted simultaneously.
- The transmit signal carrier frequencies are separated such that there is no spectral overlap between the two signals.
- Within the simulation, attenuation due to range is ignored and the signals are normalized.

3.6 Software Model

To demonstrate the methods derived previously in this chapter, a software model was developed to simulate the SAR collection process. The intent of the model is to accurately simulate the real world scenario of collecting transmitted WiMAX signals, and to use them to generate SAR images of a given target scene. An accurate model developed through incremental steps allows investigation and exploration of given SAR collection scenarios and the opportunity to study system behaviors. These scenarios can exist for a realistic environment not limited by size, and reflect the

type of scales consistent with the real world, such as receiver ranges and target scene sizes. Accurate results motivate expectations for the lab experiment and provide a foundation for further development and study.

The model was developed in MATLAB, and includes the entire process from defining a target scene and signal parameters, to generating images using the FBP algorithm. The user has the ability to define the target scene, the platform locations and the signal parameters. The simulation is run from a single script, but calls numerous functions.

3.6.1 User Defined Parameters.

The user is able to define a target scene in the (x, y, z) plane, including the scene extent and the location and amplitude of the targets. The receive aperture is also defined initially, and requires the aperture range and angle increments to build a vector of M angles. The transmit platform ranges and angles are also defined with reference to the scene center and to the receive aperture. The user is able to define the transmit signal parameters including the carrier frequencies, bandwidth, and number of data symbols within the WiMAX signal.

The remaining steps within the model are repeated for each pulse of the collection aperture. That is, the following discussion is detailed for a single pulse, but in the model the process is looped for each individual collection angle.

Based on the user definitions, the relevant parameters for a single pulse such as the bistatic angle, β , and the associated time delays are computed through a separate function. This function also generates plots of the given configuration to allow the user to ensure accuracy. The timing parameters are computed using the equations introduced in Section 3.2.

3.6.2 Signal Generation.

The user defined parameters, along with the time parameters, are passed to a function which generates both a single pulse reference signal and the return signals associated with the respective time delays. A single return signal for each bistatic pair is generated, which consists of the summation all the single pulse target returns. To generate the single pulse WiMAX signal, another function is called which constructs the WiMAX signals and the time vector corresponding to the signals. This function is developed from the same script used to generate the WiMAX signal in the OFDM experimental radar, discussed later in this chapter. This ensures consistency between the simulation and the experiment. The sampling time of the simulated signal is defined by two factors, the highest carrier frequency and the bandwidth of the respective signal given by (2.19). For a maximum carrier of 3 GHz, the sampling time is determined by 6 GHz (twice the highest carrier to ensure Nyquist criteria is met) and the bandwidth. The carrier sampling frequency can be altered within the software by the user if a higher than 3 GHz carrier is to be used.

Following the generation of the two receive signals and two reference signals corresponding to each bistatic pair, the signals are resampled to the finer of the two sampling rates, (only required if the bandwidths ensure different f_s as per (2.19)) and combined (zeropadded if required) to a common timing vector. This timing vector is defined by the higher of the two sampling rates.

3.6.3 Signal Processing Method Implementation.

In the first signal processing approach, defined by Section 3.4.1, the single receive signal $r(t)$ is the summation of the two individual receive signals, $r_1(t)$ and $r_2(t)$. The single receive signal, $r(t)$, and the respective reference signal, are then deramped and filtered at baseband following the derivation in Section 3.4.1, to produce $s_1(t)$,

$s_2(t)$, $s_{1ref}(t)$ and $s_{2ref}(t)$. Prior to the filtering step, the signals are transformed to the frequency domain using the FFT. The filter employed is a rectangular windowing function, whose upper cutoff frequency is determined by the highest frequency of the baseband signal. The size of the filter is defined by twice the highest frequency component in the baseband signal, corresponding to $\frac{B}{2}$. An example of this filter is illustrated in Figure 3.3. As well as remove the higher frequency components, the result of the filtering approach is to remove zeros in the frequency domain, which corresponds to a reduction of samples in the time domain. An added advantage of this filtering step is to reduce the computational burden. The new filtered signals consist of L fast time samples. A frequency vector of L samples is also stored, corresponding to the filtered frequencies.

Once filtered, the remaining signal $S_p(f)$ is matched filtered with $S_{pref}(f)$ to generate a vector of phase histories for the p th transmit signal, and stored in the m th location of a predefined $L \times M$ array.

This process is repeated for each pulse to generate a matrix of phase histories, \mathbf{G} .

The second signal processing approach, defined by Section 3.4.2, follows similar steps; the difference is in the deramping step, which now uses ω_{mid} as the carrier. The same filtering approach is used, but the size is now larger to account for the wider bandwidth, as illustrated by Figure 3.5.

To produce a single range profile of a given collection angle m , the inverse FFT (IFFT) can be applied to the m th column of \mathbf{G} . Figure 3.6 is an example of a range profile. This range profile was generated from the phase history created by a single target located at the scene center, at a range of 8000 m.

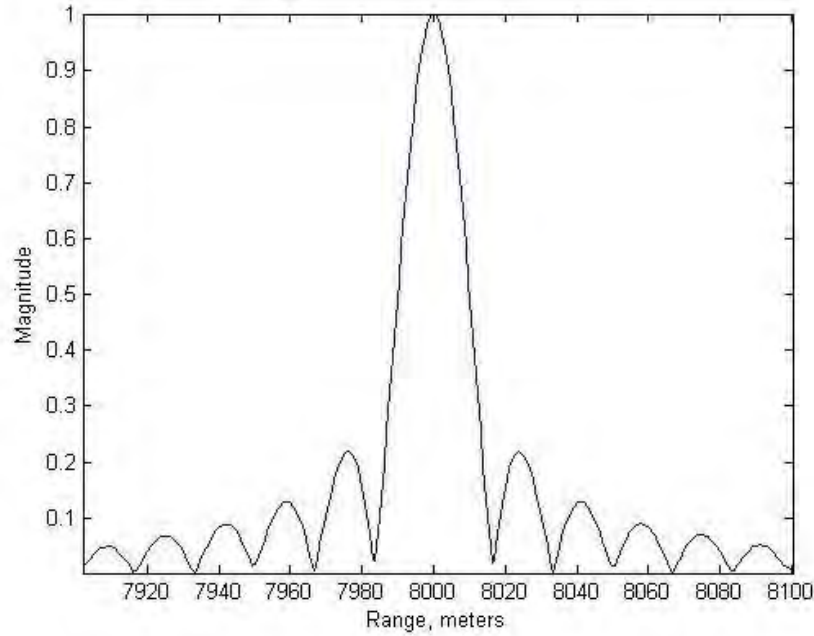


Figure 3.6. Range profile of a target at the scene center, range of 8000 m

3.6.4 Filtered Backprojection Imaging Algorithm.

The final step of the model is to produce SAR images. The input to the modified FBP imaging algorithm is the single data structure, made up of all the relevant radar and signal parameters and the respective phase histories. The same FBP algorithm is used on the data created from both signal processing methods.

When using the signal separation and parallel processing method, this algorithm applies FBP for each phase history, creating two coherent SAR images - one image from signal 1, and one from signal 2. These images are then coherently (complex values are summed) and non-coherently (magnitudes summed) combined to produce two multistatic images. Examples of this can be seen in Chapter IV.

For the second method, Figure 3.4 shows that two images are created from the single collect and processing stream. The purpose of two images from a single processing stream is to account for the geometrical differences in the two bistatic pairs.

Each transmitter will create a different bistatic aperture assuming that the two transmitters are not located in the same position in space. Therefore, the single phase history is processed twice to account for the geometric properties associated with each unique bistatic pair. When the two images are combined, it should be apparent that the target will have improved resolution in range due to an increased bandwidth, and improved resolution in cross range due to the simulated wider aperture resulting from the extent of the two transmitters.

3.6.5 Phase Error Analysis.

In order to investigate the effects of phase errors in the image, range errors are required to be introduced into the software model. This functionality is included as part of the main model and is controlled by the user. The user is able to introduce range errors in the receive aperture position and/or in the transmitter location. The error type is a function of the position in the aperture, so varies with each pulse collected. The types of errors available to the user for the receive aperture position are random, quadratic, linear, cosine, sawtooth, and constant. For the transmitter location, a constant error can be applied. The maximum value of the positional error can be varied by the user.

The error in the receive aperture is applied for each pulse collected, so as to introduce a unique phase error for each pulse. This corrupted phase history is then processed and passed to the imaging algorithm under the assumption that the flight path was constant with no error in position. This will produce simulated SAR images with errors resulting from the incorrect range determination, and allows direct observation between the type of error and effect on the image.

Once the images have been created with the corrupted phase history data using the FBP algorithm, the user has the option to correct for the error. The error type

and vector used to create the phase history are stored in the same data structure that is passed to the algorithm as defined in Section 3.6.4. The imaging algorithm applies the inverse filtering technique explained, in Section 2.3.6, to each sample within the corrupted phase history prior to applying FBP and generating an image. The user is able to define the error value of each pulse based on selecting increments to approximate the total range error.

The corrected error value for a given pulse m given by $r_\epsilon(m)$, is the mean error over a user defined sample size. For example, for a step size of 4, and aperture of $-20:20^\circ$, the mean positional error is computed over pulses $-20:-17^\circ$, and the value is used as the correction for each of these four pulses in the phase history. The same method is applied for pulses from azimuths $-16:-13^\circ$ and so on. Figure 3.7 illustrates this concept for a quadratic type error.

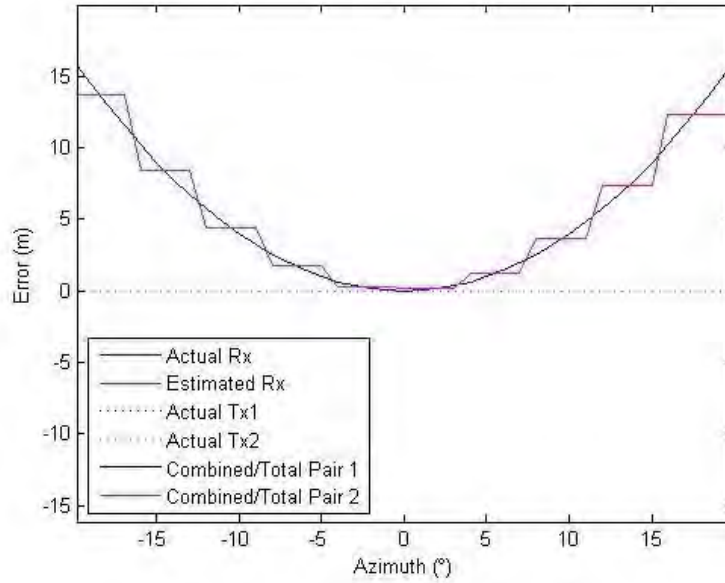


Figure 3.7. Phase error correction plot

In this example, a mean error of 14 m is applied for pulses collected over $-20:-17^\circ$. For an increment of 1, the corrected error vector is an exact estimation of the error used to generate for the phase history collection. The finer the step size, the better

the level of error correction in the image is expected.

3.7 Experimental Collection

In order to validate the methods described, and the accuracy of the software model, experimental data was collected using the AFIT experimental OFDM radar developed by Gutierrez [12]. The experimental radar can be configured to transmit a single pulse WiMAX signal, or transmit dual pulses using different carriers over two spatially diverse antennas.

3.7.1 Equipment System Description.

The experimental OFDM radar consists of commercial off the shelf items controlled through MATLAB graphical user interfaces (GUIs). The components of the radar can be seen in Figure 3.8.

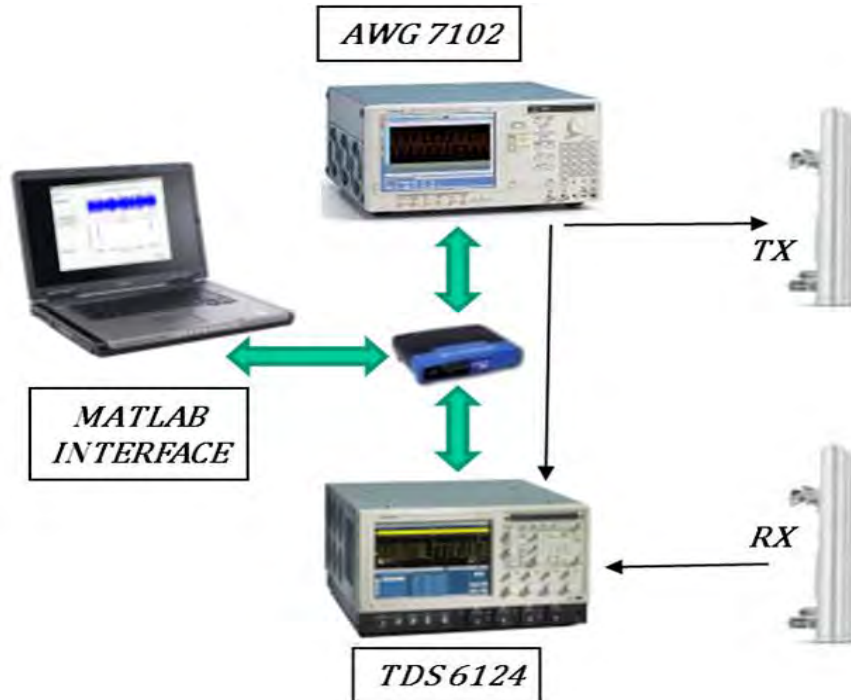


Figure 3.8. Experimental OFDM radar

The transmitter source is a Tektronix AWG7102 arbitrary waveform generator (AWG). The AWG output is connected to a Mini-Circuits ZKL-2R7 amplifier which is fed into a WA5VJB Log Periodic Antenna (LPA). The LPA frequency range is 900-2600 MHz; the antenna can be seen in Figure 3.9. The AWG is capable of transmitting two signals on channel 1 and 2 simultaneously, and this capability was exploited in the multistatic configuration, where two separate transmit chains were used. The receiver chain consists of the same type LPA which is fed into a Tektronix TDS6124 digital storage oscilloscope (DSO). The control of the radar is performed via MATLAB, with all components communicating through a wired local area network (LAN) hub.

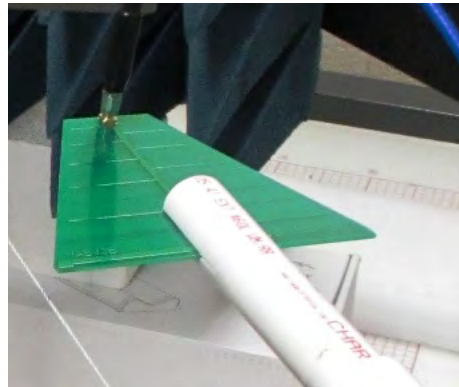


Figure 3.9. 900-2600 MHz LPA

The MATLAB interface consists of a series of GUIs. The first GUI, seen in Figure 3.10, is used to create a given OFDM signal. A generic OFDM, or a specific WiMAX, waveform can be created through a selection of different signal parameters. Once the signal is created via this GUI, it is then stored so as to be selected for the radar signal. Both the time domain and frequency domain representation of the given waveform is displayed.

The radar control itself is conducted through the second GUI, seen in Figure 3.11. This GUI controls the transmission and collection of the loaded waveform, as well as the configuration of the AWG and the DSO. Once the waveform is created in the first

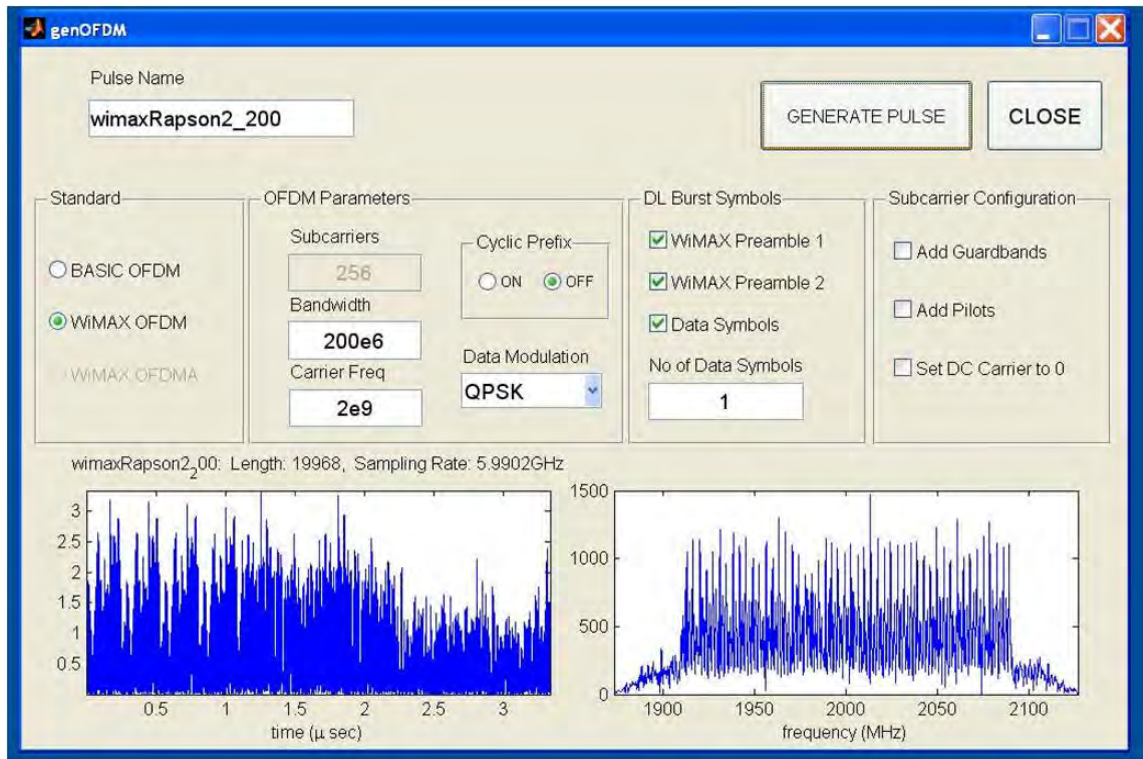


Figure 3.10. MATLAB waveform generator GUI

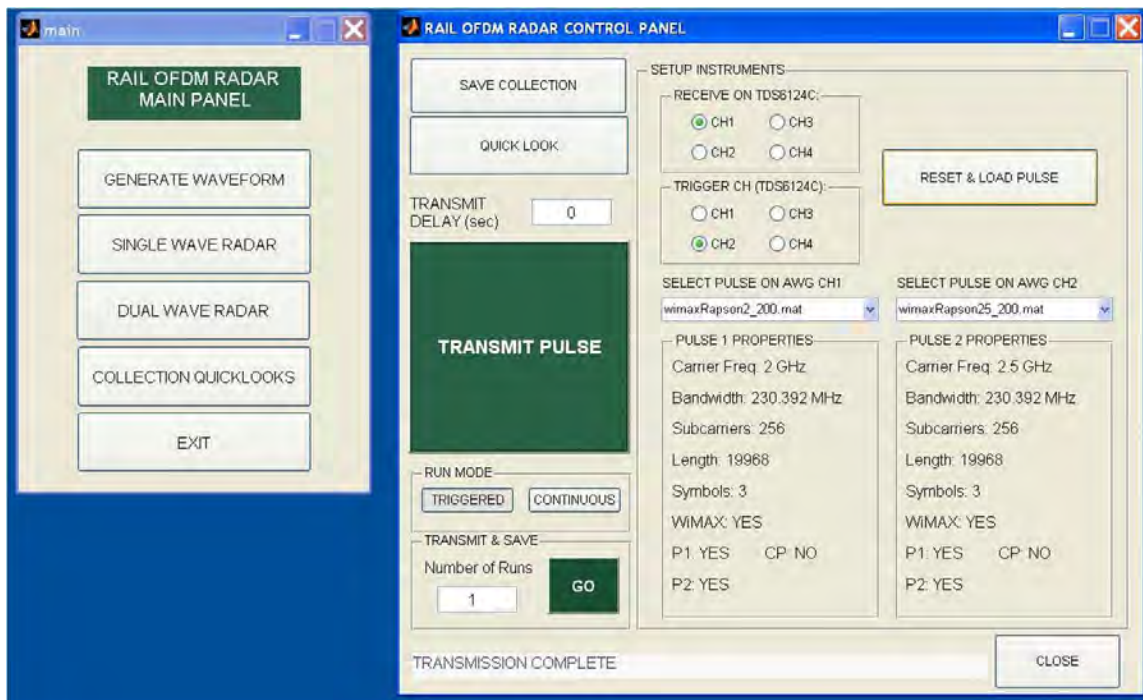


Figure 3.11. MATLAB Radar Control GUI

GUI, it can be selected in the second GUI and loaded to the AWG for transmission. Once the AWG has the relevant waveforms loaded on the correct channels, a single pulse can be transmitted from both channels at the same time. A second output is sent to the DSO as a trigger to capture a specified window of time. The received signal is then displayed on the DSO, from which the data can be saved and stored in a MATLAB compliant format for post processing. This data contains the signal vector, the sampling frequency and length of signal.

3.7.2 Experimental Radar Configuration and Data Collection.

The experimental collection was conducted within the AFIT Radar Instrumentation Laboratory (RAIL) using a multistatic setup of two transmitters, a single receive antenna and two targets placed at the scene ‘center’. The initial data collection involved a single bistatic pair of one transmitter and one receiver to ensure that bistatic data collection was possible. Once established, a second transmitter was added to the experiment. The OFDM radar was configured such that a single pulse was transmitted and the received signal stored within MATLAB using the capabilities explained in Section 3.7.1. Figure 3.12 shows the experimental setup of the radar for the multistatic collection.

As a single point target did not provide a strong enough signal return, a large flat plate antenna was used to mimic a single point target. For every position in the collection aperture, the plate target would be orientated toward the bisector angle to provide a consistent target. Figure 3.12 demonstrates that a single plate target was used for each bistatic pair. For the entire data collect, the distance between the transmitter-target-receiver remained the same for both pairs, mimicking a single point target for the entire collect. Radar absorbent material was placed directly behind the targets to suppress unwanted returns from the background and to ensure

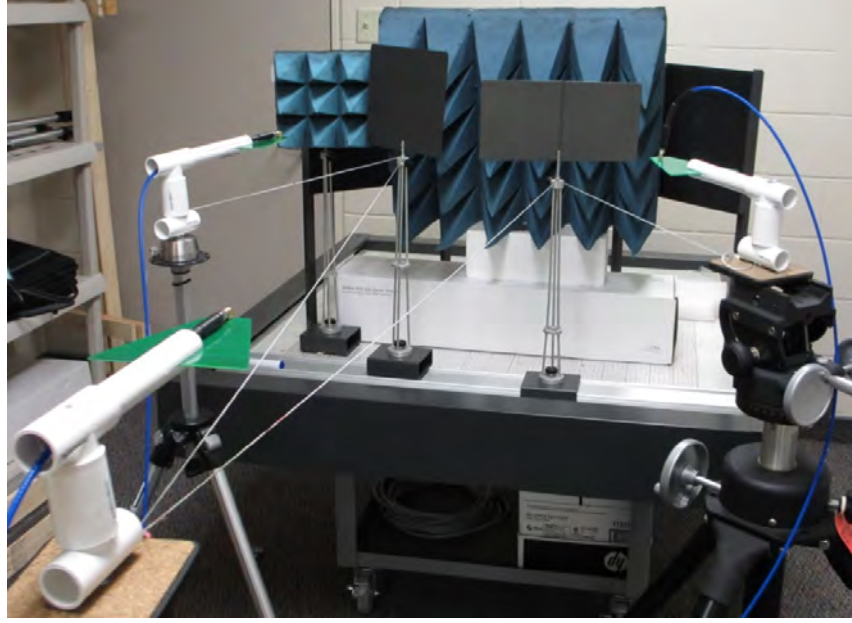


Figure 3.12. Multistatic experimental configuration

only returns from the target were collected at the receiver.

The parameters of the signals used for the experiment are detailed in Table 3.1. The transmitters were placed close to the targets to narrow the returns from surrounding objects and to maximize the return at the receiver.

Table 3.1. Experimental radar parameters

	Transmitter 1	Transmitter 2	Receiver
Range (m)	0.25	0.25	1.10
Θ ($^\circ$)	35, 25	-25, -35	
Aperture ($^\circ$)			-20:2:20 -30:3:30
f_c (GHz)	2, 2.2	2.5	
Bandwidth (MHz)	200	200	

Figure 3.13 illustrates the multistatic geometric angles for the experimental collection.

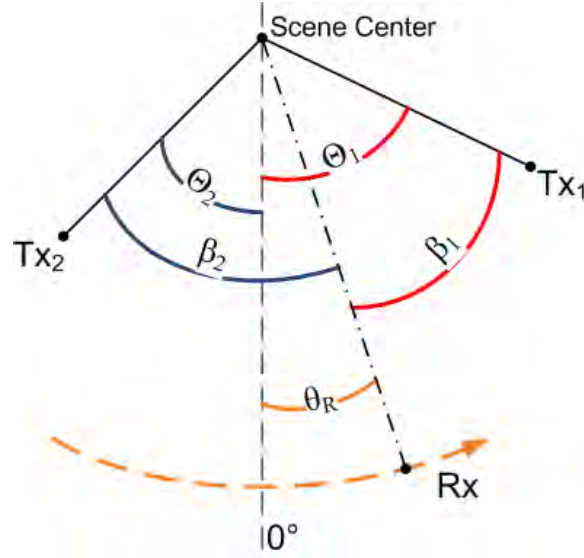


Figure 3.13. Experimental multistatic geometry

The procedure for the experimental data collection is as follows:

1. Set up the transmitter locations and connect to the correct channels on the AWG. Move the receiver antenna to the first position in the aperture. Position the plate targets orientated towards the bisector angle. Figure 3.14 shows one of the plate targets used throughout the collection.
2. Define the two WiMAX signals in the MATLAB waveform generator GUI and ensure correct waveform parameters through plots.
3. Load the two WiMAX waveforms to the AWG using the MATLAB radar control GUI. Ensure the AWG and DSO are connected via the trigger. Transmit the two signals through the MATLAB GUI.
4. Observe the receive signal at the DSO and adjust the scale as required. Repeat step 3 until receive signal on the DSO is of a sufficient scale.
5. Store the single receive signal via the radar control GUI once scale is adjusted.

6. Move the receiver to the next position in the aperture and reposition the plate targets. Repeat steps 3 and 5.
7. Repeat step 6 until the entire aperture collection is complete.
8. Set up a single bistatic pair separated by the distance to the scene center. Transmit a single preamble signal using the MATLAB GUI and store the received signal. This signal becomes the reference signal.

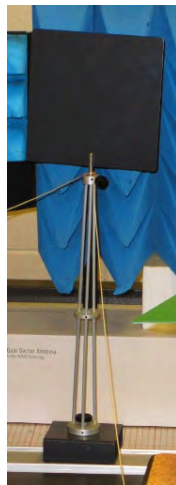


Figure 3.14. Plate target used for experimental collection

For the data collection scenarios, the receiver was moved in increments of between 2° and 3° . At each position in the aperture, the single receive signal was stored, creating a vector of 200000 fast time samples. The time between samples was set to 500 ns. Once the aperture collection was complete, a single reference signal for each carrier frequency was collected by storing a received signal, with a distance of 1.35 m between the transmit and receive antennas, as per step 8. This provided the respective reference signal to the scene center.

3.7.3 Data Processing and Image Generation.

Using different combinations of configurations defined by Table 3.1, numerous sets of measured data were collected. The specific data collection parameters are detailed in Chapter IV. The next step was to develop a script in MATLAB to generate images using the measured data. Using the software model as a foundation, each of the measured data vectors and reference signals are deramped to baseband and transformed into the frequency domain. The signals are then filtered around 0 Hz prior to being matched filtered and stored in a predefined phase history array.

Once the phase histories are generated, they are allocated to a data structure which includes all the relevant radar configuration parameters for that data collection, including both the geometric and signal parameters. This data structure is of the same format as the data structure used in the software model, and is therefore input directly into the same FBP imaging algorithm, ensuring the same imaging algorithm in Section 3.6.4 is used for both the simulated and experimental data.

3.8 Chapter Conclusion

This chapter detailed the methodology for developing and validating methods for producing SAR images using WiMAX signals. It presented the mathematical definitions of the geometric and signal models before presenting mathematical derivations of two proposed signal processing models. In order to validate and demonstrate the theoretical models, a software simulation model using MATLAB was explained. To demonstrate the simulated model a step further, an experiment was presented to collect physical measurements of the WiMAX signal using the AFIT developed experimental OFDM radar. The results of the simulation model and the experimental data collection are presented in the next chapter.

IV. Results

4.1 Chapter Overview

This chapter presents the results of the simulations and experiment discussed in the previous chapter. Given the nature of the research, the results of the software models and experiment are simulated SAR images. Comparisons between theoretical, simulated and measured results are made, with both qualitative and quantitative analysis provided where possible. The chapter first explains the simulation model results and images generated using both signal processing approaches. The second half of the chapter looks at the images created from the experimental data collection, including a brief comparison with the images created using the software model.

4.2 Simulation Results

4.2.1 2D and 3D Simulation Validation.

The simulation was built in incremental steps. The first major goal was to ensure that the model detailed in Section 3.6, for the signal processing method described in Section 3.4.1, was generating SAR images which reflect a given target scene. Initially, the simulation used a 2D model, so there were no z components in the platform or target locations. Figure 4.1 provides an example of the initial simulation geometry used, demonstrating both the stationary transmitter locations and the receiver platform aperture in the (x, y) plane. Figure (b) shows two targets at locations $(0, 0)$ and $(40, 20)$, noting that the y dimension is cross range and the x dimension is range.

Given the above configuration, the images in Figure 4.2 were generated using the software model and FBP algorithm detailed in Chapter III. These two images represent the coherently combined images from both transmitters. Figure (a) is an image generated from the two transmit signals having a bandwidth of 100 MHz,

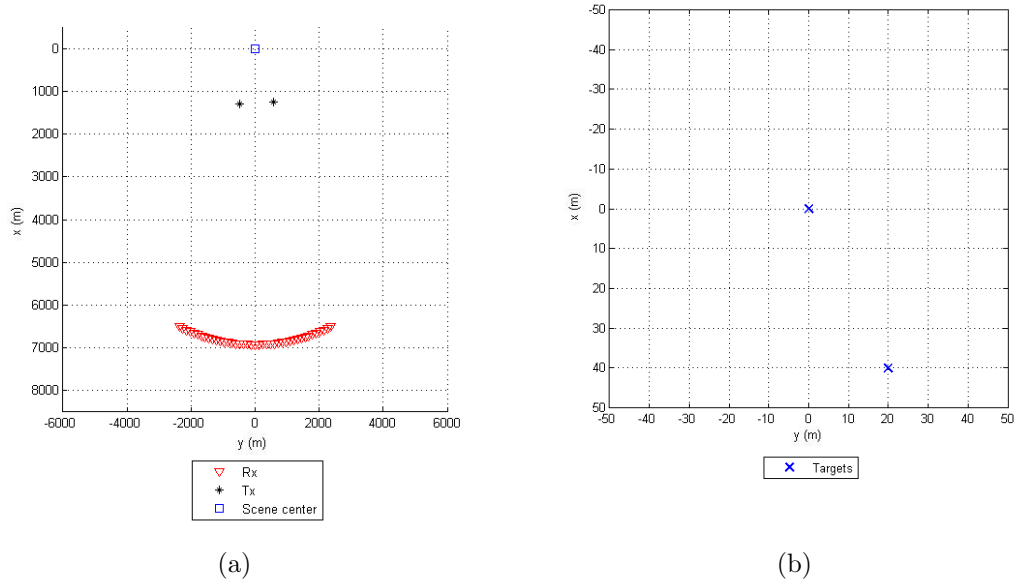


Figure 4.1. 2D model simulation geometry (a) Radar configuration (b) Target scene

while Figure (b) is created using two signals of 20 MHz bandwidth. It is clear from Figure 4.2 that the images consist of two targets, one at the scene center and the other at the correct location of (40, 20). By observing the images, it is evident that the larger the bandwidth, the finer the resolution in range. The finer range resolution affects the cross range resolution as well, resulting from the filtering step in the signal processing approach.

4.2.2 Simulation Image Analysis.

Following the validation of the initial code, the software model was expanded to include the altitude, or z component. Figure 4.3 illustrates the 3D model geometry. The receiver aperture now exists with some altitude component, as do the two transmitters. The target scene, represented by the blue square, is located on the ground centered at (0,0,0). All of the remaining images analyzed and presented in this chapter are generated using this 3D model.

In order to generate sufficient data and images for analysis, a range of parameters

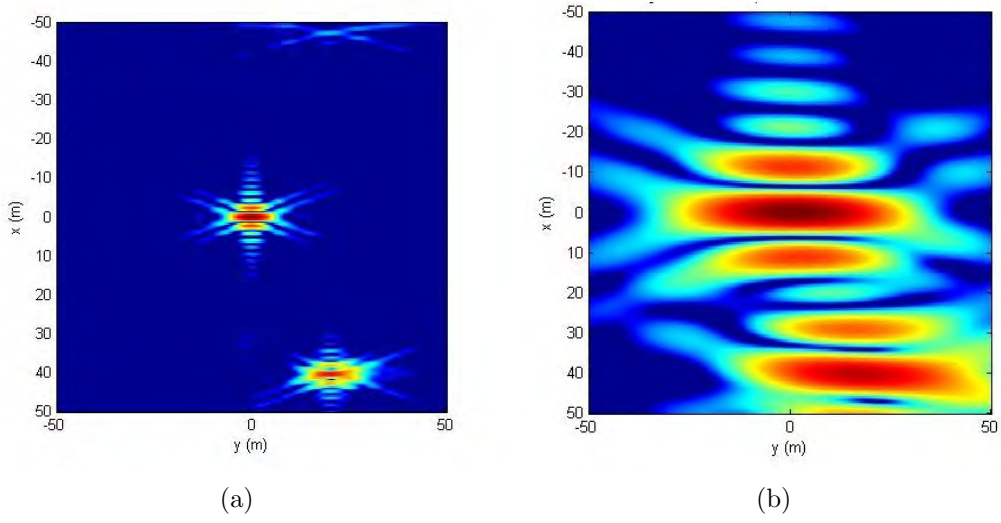


Figure 4.2. Combined SAR images with two targets, signal bandwidths of (a) 100 MHz
(b) 20 MHz

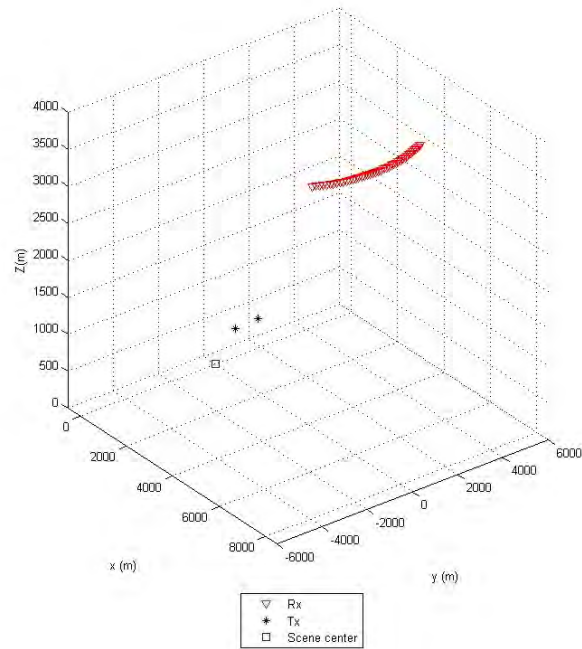


Figure 4.3. 3D simulation geometry example

were used, and those used throughout the simulations are listed in Table 4.1. The simulations do not only capture images to compare to the experimental data, but also explore additional parameters to add some diversity to the results, and produce further data to analyze. The images are created for a single point target, placed

at the scene center. For the purposes of analysis, the resolution is measured as the 3 dB beamwidth of the main lobe in the image. A finer resolution implies a narrower beamwidth in the respective dimension.

Table 4.1. Simulation parameters

	Transmitter 1	Transmitter 2	Receiver
Range (m)	1600	1600	8000
Θ angle ($^{\circ}$)	-10, -20, -40	10, 20, 40	
Rx Aperture ($^{\circ}$)			-10:10 -20:20 -30:30 -40:40
f_c (GHz)	2	1, 2.2, 2.4, 2.5	
Bandwidth (MHz)	100, 200	100, 200	

Figure 4.4 illustrates the colorbar scale used throughout this chapter for each of the images.

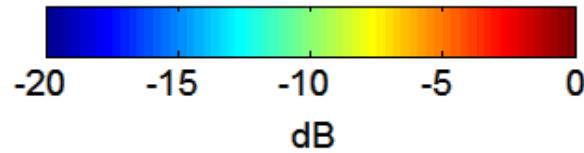


Figure 4.4. Colorbar image intensity scale

The initial analysis provided is qualitative based on observations prior to a more quantitative approach for the simulation images used in comparing data to the experimental results and the images created from the second method. The purpose of this is to ensure accuracy of the simulation and define a foundation for further image analysis. Sections 4.2.3 and 4.2.4 include images generated through the signal separation and parallel processing method, while Section 4.2.5 looks at the simulated images from the second combined reference signal method. For all simulations and

collections, the receiver aperture was centered on 0° , and the angles of Θ are with respect to the center of the receive aperture.

4.2.3 Bandwidth and Aperture.

The first analysis compares the effect of the WiMAX signal bandwidth and the collection aperture on the target within the image. Figure 4.5 shows the images generated from signal 1, transmitted at 2 GHz, and processed using the signal separation approach. The transmitter for signal 1 is located at -40° from the center of the receiver aperture.

The target response is observed to be oriented towards half the transmitter angle,

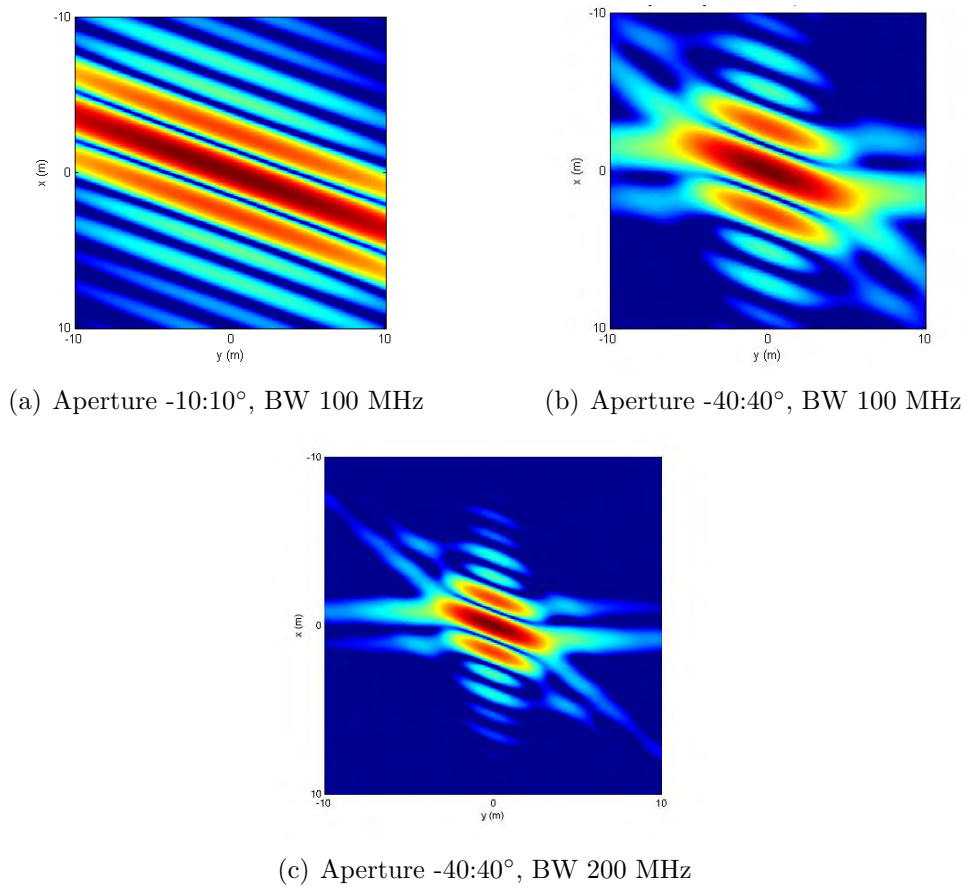


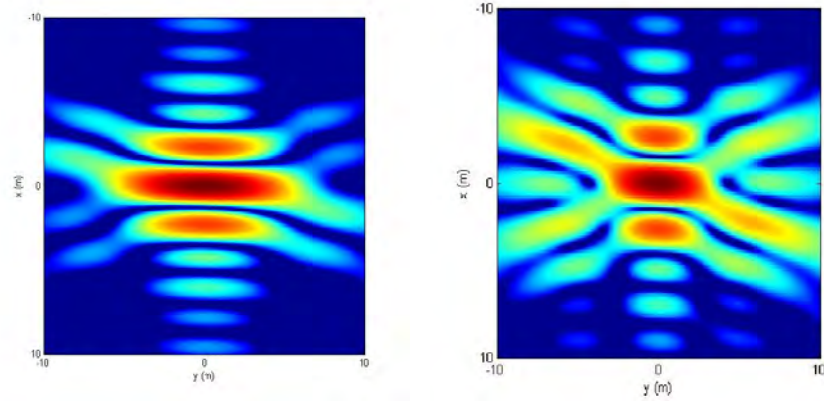
Figure 4.5. SAR images from different apertures and bandwidths for Signal 1 @ 2 GHz located at -40°

Θ_1 of the first bistatic pair. This is the result of the effective aperture being centered on the bisector angle. As the collection aperture increases, so does the improvement in cross range resolution. Similarly, as the bandwidth doubles in size, the range resolution improves. That is, a finer target main lobe along the x-dimension is seen in the image. These observations are consistent with the expressions outlined in Section 2.3.3. The images created from Signal 2 at a different carrier frequency demonstrate the same characteristics, however, the target response is oriented toward the second bisector angle, $\frac{\Theta_2}{2}$.

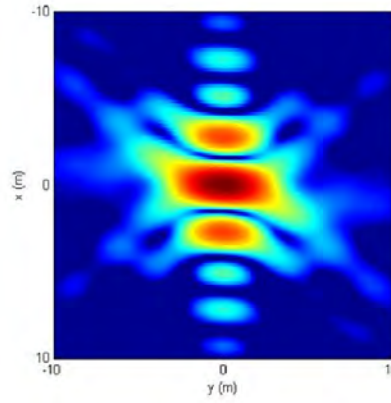
4.2.4 Effective Bistatic Apertures.

The next analysis looks at the effect of different collection apertures on the image. For these images, the carrier frequencies are 1 GHz and 2 GHz respectively, both with a signal bandwidth of 100 MHz. Figure 4.6 shows the images created from the various aperture combinations. Figure (c) shows an increase in the effective aperture by a factor of 2 over Figure (a), which corresponds to finer resolution by a factor of 2. The measured resolution improvement between (a) and (c) is approximately 2, that is, the cross range resolution beamwidth value in (c) is half that in (a).

Figure (b) demonstrates the effect of ‘gaps’ within the collection aperture. The concept of ‘gaps’ within the collection is illustrated by Figure 4.7, and indicates narrower bistatic apertures for each bistatic pair. The ‘gaps’ are caused by the single bistatic aperture extent being narrower than the bistatic angle of the respective transmit/receive pair. A full aperture consists of data between all the angles within aperture extents as seen in Figure 4.7 (b). Where Θ is large enough to produce gaps in the data, as illustrated by Figure 4.7 (a), then artifacts begin to appear in the image. These artifacts are the result of the coherent addition of the sidelobes of one signal with the main beam of the other.

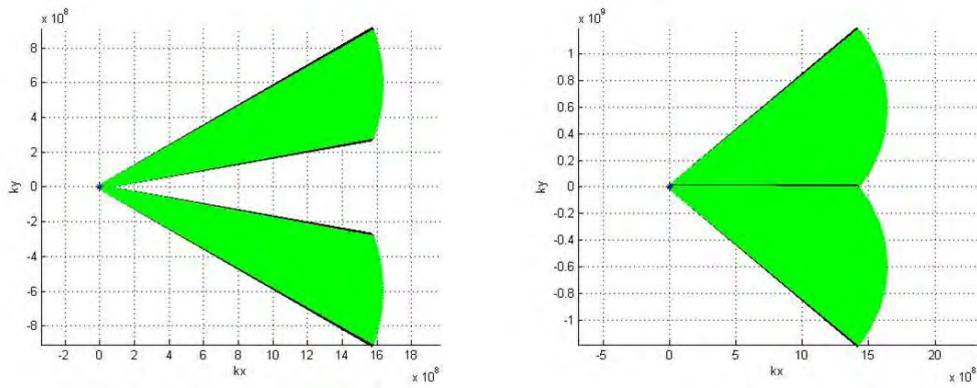


(a) Txs @ $\pm 20^\circ$, Rx Aperture $-20:20^\circ$ (b) Txs @ $\pm 40^\circ$, Rx Aperture $-20:20^\circ$



(c) Txs @ $\pm 40^\circ$, Rx Aperture $-40:40^\circ$

Figure 4.6. Coherent combined SAR images of 100 MHz bandwidth with varying effective apertures



(a) Gaps

(b) No gaps

Figure 4.7. Collection apertures in the spatial frequency domain

The gaps in the aperture are analogous to zero information between pulses within a pulse train, where each individual aperture represents a single ‘pulse’ of information. Sampling theory defines an inverse relationship between the spatial and frequency domains. The Fourier transform of a series of rectangular pulses in the spatial domain is a series of sinc functions separated by the pulse repetition frequency (PRF). The greater the PRF, the smaller the space of zero information between pulses in the spatial domain, and the greater the sinc functions are separated in the frequency domain [21]. The inverse Fourier transform of two rectangular pulses in the frequency domain is two sinc functions in the spatial domain. In a similar manner, the greater the amount of zero information (greater spacing) in the frequency domain, the closer the sinc functions are in the spatial domain. This leads to higher amplitude sinc functions which result in closer responses around the main lobe within the spatial domain, or in this case, the image.

The extent of the angular diversity between the transmitters used to create Figure 4.6 (b) and (c) is the same, $\pm 40^\circ$, and the receiver aperture is centered on 0° , which results in the same bistatic angle diversity in both configurations. However, the single signal images from the configuration in (c) have a narrower individual main beam resolution resulting from an increased receiver aperture. This concept is demonstrated in the Section 4.2.3.

Figure 4.8 shows images generated from the same parameters used to generate Figure 4.6 (a) and (c); the difference being the signal bandwidth of both signals is now 200 MHz, vice 100 MHz. When comparing the four figures, Figure 4.6 (a) and (c), Figure 4.8 (a) and (b), it is evident that the range resolution is improved by the increased bandwidth, and the cross range resolution is improved by the larger aperture sizes.

The theoretical range resolution for the 100 MHz bandwidth (accounting for the

increase in sampling factor), is approximately 1.3 m. The measured resolution from the image is 1.45 m. The 200 MHz bandwidth image resolution is measured to be 0.7 m compared to the theoretical 0.65 m.

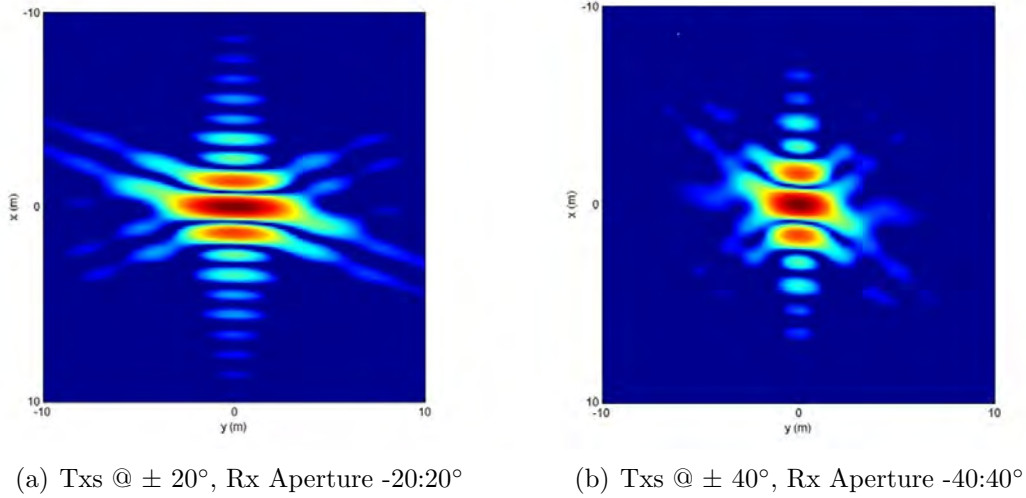


Figure 4.8. Coherent combined images for different effective aperture

Figure 4.9 illustrates the resulting coherent combined image if there is negligible diversity in the transmitter bistatic angles.

The receiver aperture is $-30:30^\circ$, and the two transmitters are located at $\pm 10^\circ$. The orientation of the target still exists at the respective bisectors, however, the combined image cross range resolution is only improved by a factor of less than 10% when compared to the individual images. This is minor compared to the significant improvements made by the larger angular extents. Therefore, as expected, the bistatic angle diversity determines the improvement in the cross range resolution of the combined images.

4.2.5 Combined Reference Signal Images.

The next set of images was created from the phase histories generated using the second signal processing method. By using the entire bandwidth defined by the

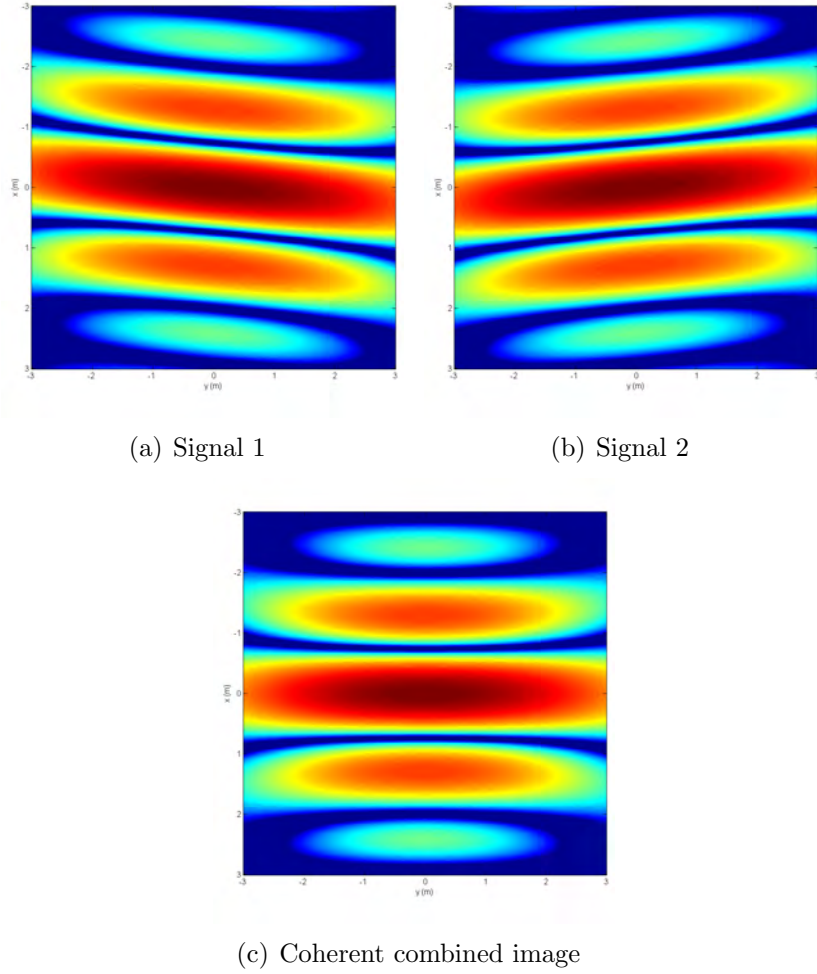
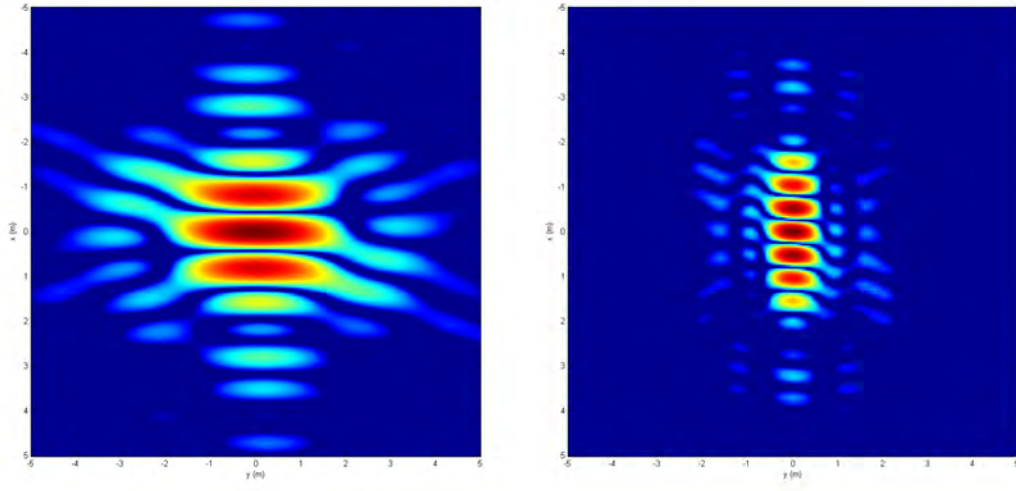


Figure 4.9. SAR images using signal separation method. TxS @ $\pm 10^\circ$, Rx Aperture $-30:30^\circ$

separation of the two carrier frequencies, it is expected that the range resolution will improve. Recall the expression for the bandwidth extent is defined by (3.16).

Figure 4.10 shows the images generated using the combined reference signal model. These images are coherent combined images, therefore already account for the geometric diversity of the transmitters. It is evident a larger signal carrier separation, and therefore the greater bandwidth extent, leads to a finer resolution of the target for the same collection aperture, as expected. However, the amplitude of the sidelobes is significantly increased such that on initial inspection, it is difficult to ascertain a

single target within the image.



(a) $f_1 = 2 \text{ GHz}$, $f_2 = 2.2 \text{ GHz}$

(b) $f_1 = 2 \text{ GHz}$, $f_2 = 2.4 \text{ GHz}$

Figure 4.10. Coherent combined images for different carrier frequency separation. Txs @ $\pm 20^\circ$, Rx Aperture $-20:20^\circ$, Signal bandwidth 100 MHz

Figure 4.11 provides an example of the same signal parameters as in Figure 4.10(a), however, the collection aperture is greater. The same improvement in cross range resolution is obtained and is consistent with observations in the previous sections.

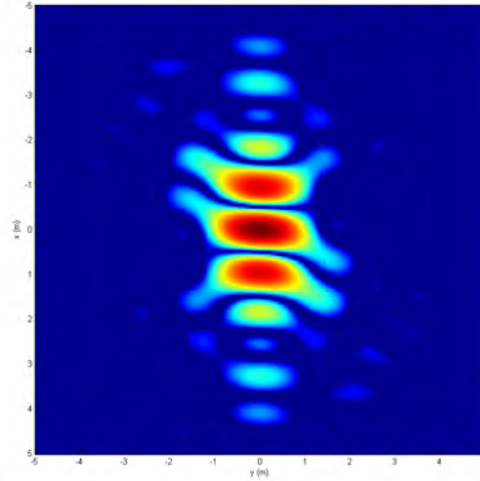


Figure 4.11. Coherent Combined Image for $f_1 = 2 \text{ GHz}$, $f_2 = 2.2 \text{ GHz}$, Rx Aperture $40:40^\circ$, Txs @ $\pm 40^\circ$, Signal bandwidth 100 MHz

Based on the observations from the increased signal separation, further analysis is conducted on the range resolution measurements and the sidelobe levels.

The two carrier frequencies were initially separated by the minimum value such that there was no overlap between the bandwidths of the signals. This minimizes the zero values between the two signals, and this separation was used as the baseline for further measurements.

Table 4.2 lists the separation of the two carriers and the corresponding bandwidths resulting from the separation. Signal 1 carrier frequency was kept constant at 2 GHz, whilst the carrier for signal 2 was incremented by 10% of the bandwidth.

Table 4.2. Signal separation and bandwidth extent (MHz)

Increment		1	2	3	4	5	6	7	8	9	10
20 MHz	Separation	28	30	32	34	36	38	40	42	44	46
	BW	54	56	58	60	62	64	66	68	70	72
100 MHz	Separation	140	150	160	170	180	190	200	210	220	230
	BW	268	278	288	298	308	318	328	338	348	358
200 MHz	Separation	280	300	320	340	360	380	400	420	440	460
	BW	533	553	573	593	613	633	653	673	693	713

The first set of carriers for signal 2 were 2.028, 2.14 and 2.28 GHz for the 20, 100 and 200 MHz bandwidths respectively, leading to separations of 28, 140 and 280 MHz respectively. These carriers represent increment 1. The separation between the carriers was then incremented in steps of 10% of the signal bandwidth. When using 100 MHz signals, an increment of 10 MHz was used to separate the frequency between the carriers of the signals. Figure 4.12 illustrates the concept of moving the second signal in increments represented by k .

Figures 4.13 and 4.14 illustrate the theoretical and measured resolution for the signal bandwidths given by 200, 100 and 20 MHz. In all three plots, the measured

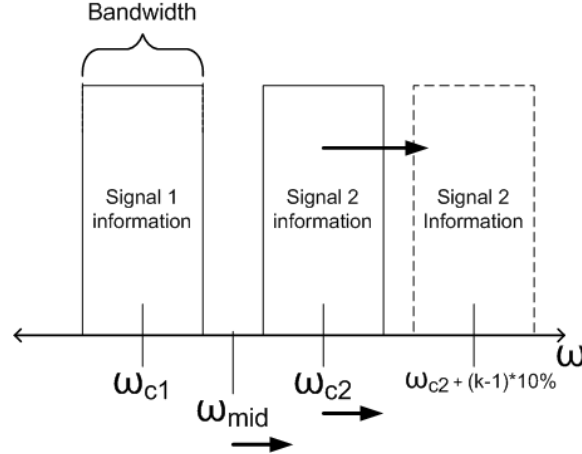


Figure 4.12. Carrier separation in the frequency domain for the k th increment

range resolution is slightly larger than the theoretical, until increment 6. Increment 6 represents 50% of the signal bandwidth from the baseline measurement, or 50 MHz for the 100 MHz signal. Therefore, for a 100 MHz signal, increment 6 is 318 MHz, or 50 MHz + 268 MHz (baseline separation). Increment 6 also represents a bandwidth separation slightly less than twice the original signal bandwidth in all three cases.

Figures 4.15 and 4.16 illustrate the normalized sidelobe amplitudes for the images generated using signals of 100 MHz and 20 MHz bandwidth respectively.

These plots represent a cut of the image along the range dimension. The main lobe is centered on 0 m, whilst the sidelobes in both plots vary depending on the signal separation. The separation between the two carriers is given by the legend. Figure 4.15 displays the sidelobes associated with separations incrementing from 150 to 230 MHz, or the even numbered increments within Table 4.2. As the signal separation increases, the main lobe 3 dB beamwidth becomes finer, as do the sidelobes whose level also increase. The same result is observed in Figure 4.16, corresponding to 20 MHz signals. Increment 6, which represents the cross over point of accurate theoretical and measured range resolution, corresponds to a sidelobe level of approximately -2.5 dB in both the 100 and 20 MHz images.

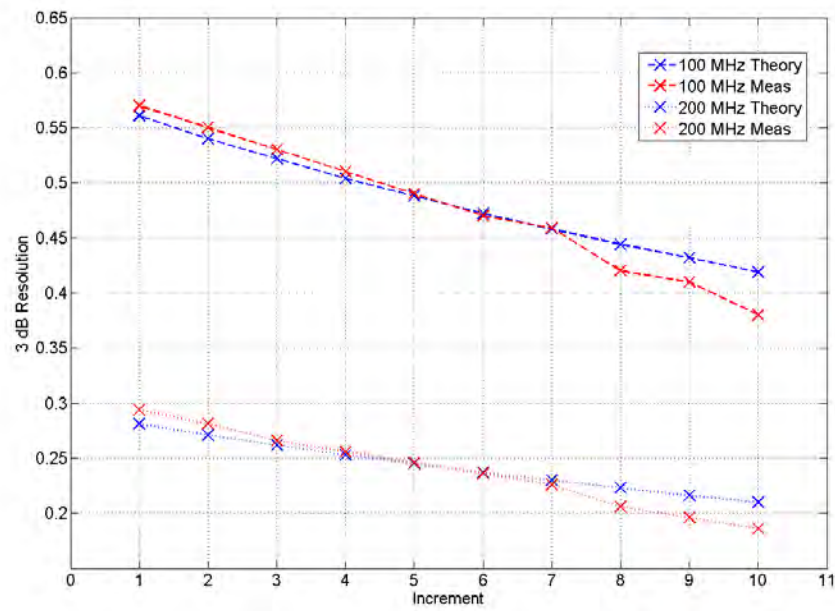


Figure 4.13. Theoretical vs measured range resolution as a function of carrier signal separation for signal bandwidths of 100 and 200 MHz

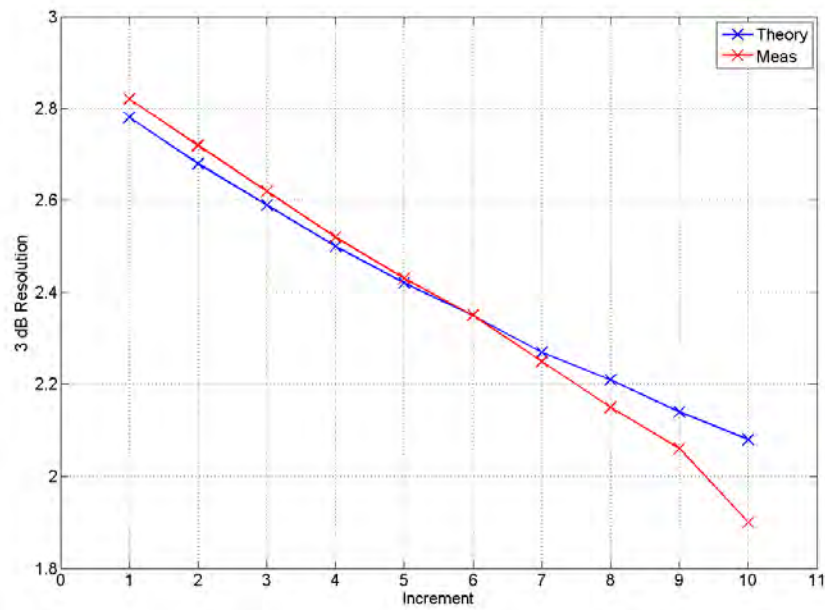


Figure 4.14. Theoretical vs measured range resolution as a function of carrier signal separation for signal bandwidth of 20 MHz

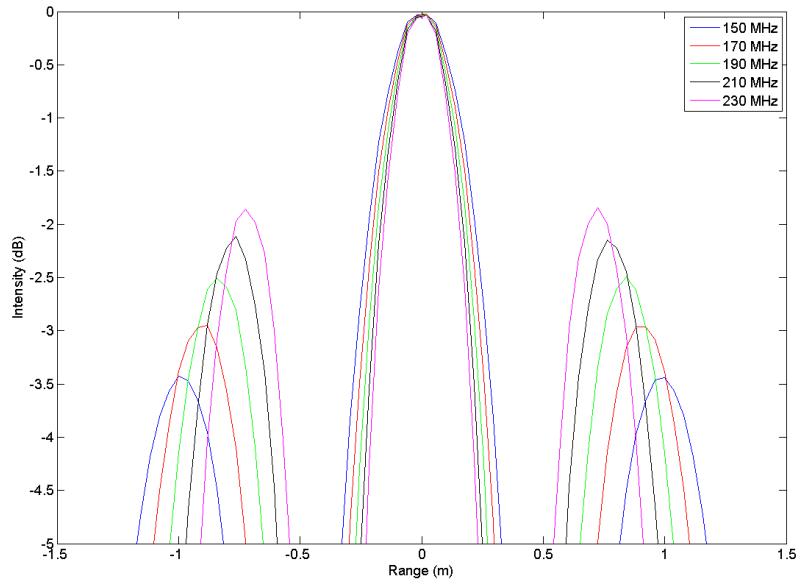


Figure 4.15. Sidelobes in range as a function of signal separation, 100 MHz bandwidth

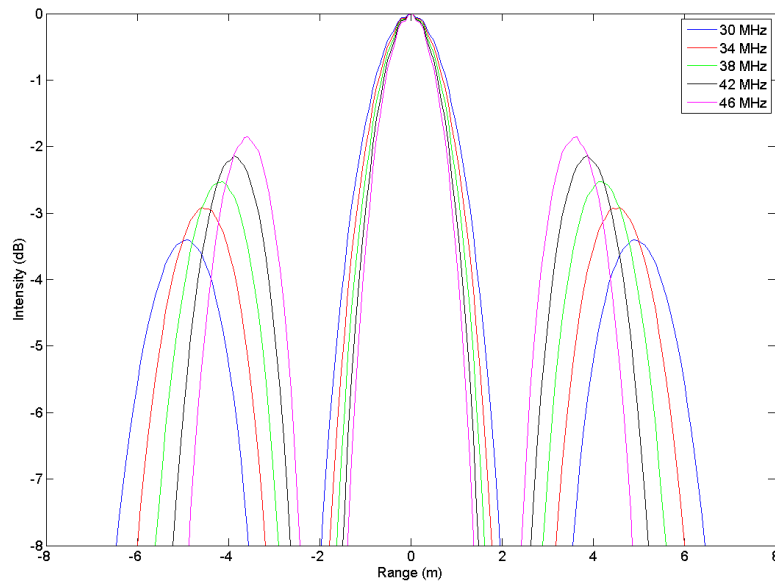


Figure 4.16. Sidelobes in range as a function of signal separation, 20 MHz bandwidth

Table 4.3 lists the average sidelobe level of each increment. The level is averaged over the same increments for each of the images created from the three different signal bandwidths. As the increments increase, and the separation becomes larger,

the sidelobe level increases. The increase in sidelobe level is due to the processing of the signals, and is explained by sampling theory detailed in Section 4.2.4. The signals consist of two pulses, or rectangular functions, now separated by some ‘gap’ of information between them. Therefore, the inverse Fourier transform of two rectangular functions in the frequency domain is two sinc functions, spaced by the inverse of the separation in the frequency domain. The greater the separation of pulses in one domain, the smaller the separation of the sinc functions in the other domain, and therefore gives the appearance of higher sidelobes.

Table 4.3. Sidelobe level (dB)

Increment	1	2	3	4	5	6	7	8	9	10
20 MHz	-3.65	-3.3	-3.2	-2.9	-2.7	-2.54	-2.3	-2.19	-2	-1.86
100 MHz	-3.74	-3.4	-3.2	-3	-2.75	-2.5	-2.36	-2.18	-2	-1.86
200 MHz	-3.7	-3.45	-3.22	-2.97	-2.76	-2.52	-2.4	-2.19	-2.02	-1.86
Avg SL level	-3.7	-3.38	-3.21	-2.96	-2.74	-2.52	-2.32	-2.19	-2.01	-1.86

Factors such as the sidelobe level may influence the effectiveness of using the combined reference signal method for signal processing. Selecting two signals with carriers separated by twice the signal bandwidth, or more, leads to a much improved range resolution, but also leads to a significant increase in sidelobe levels such that a target becomes ambiguous within the sidelobes and its exact location is difficult to discern.

4.3 Phase Error Analysis

This section presents the images created in the presence of range measurement errors defined by Section 3.6.5. The errors will include linear, quadratic and random. Only the images from signal 1 and the coherent combined image are presented in this section. Each image pair will display the image created from the corrupted phase history data, and also the image created from the corrected phase history. Each of the images created was from transmitters located at $\pm 20^\circ$ and a receiver aperture of $-20:20^\circ$. The signal bandwidth was 100 MHz.

Figure 4.17 shows the images created both before, and after, the inverse filtering linear error correction is applied. The error applied in the collection is a linear function from 0 m at -20° increasing to 10 m at 20° . The linear error is seen to produce a shift of the main target lobe in cross range along the range contour perpendicular to the bisector. This occurs in both signal images (only signal 1 is shown) such that the combined image is no longer centered on $(0, 0)$, but is a coherent addition of the two shifts in the individual images. Applying the inverse error correction on both signal phase histories corrects for this linear error, see (b), and the effect on the combined image is a single point target located at the scene center.

Figure 4.18 shows the images of signal 1 created both before, and after, the inverse filtering quadratic error correction is applied. The error applied in the collection is the same function seen in Figure 3.7; an error of 0 m at 0° , and a maximum error of 15 m at the aperture extents. The quadratic error is shown to produce a smearing, or spreading, of the main lobe in the cross range dimension along the range contour. Again, the inverse filtering technique is able to correct for this smearing, and focus the image for the single target at the scene center. The greater the increment level, the better the focusing of the image is observed.

Figure 4.19 shows the coherent combined images created both before, and after,

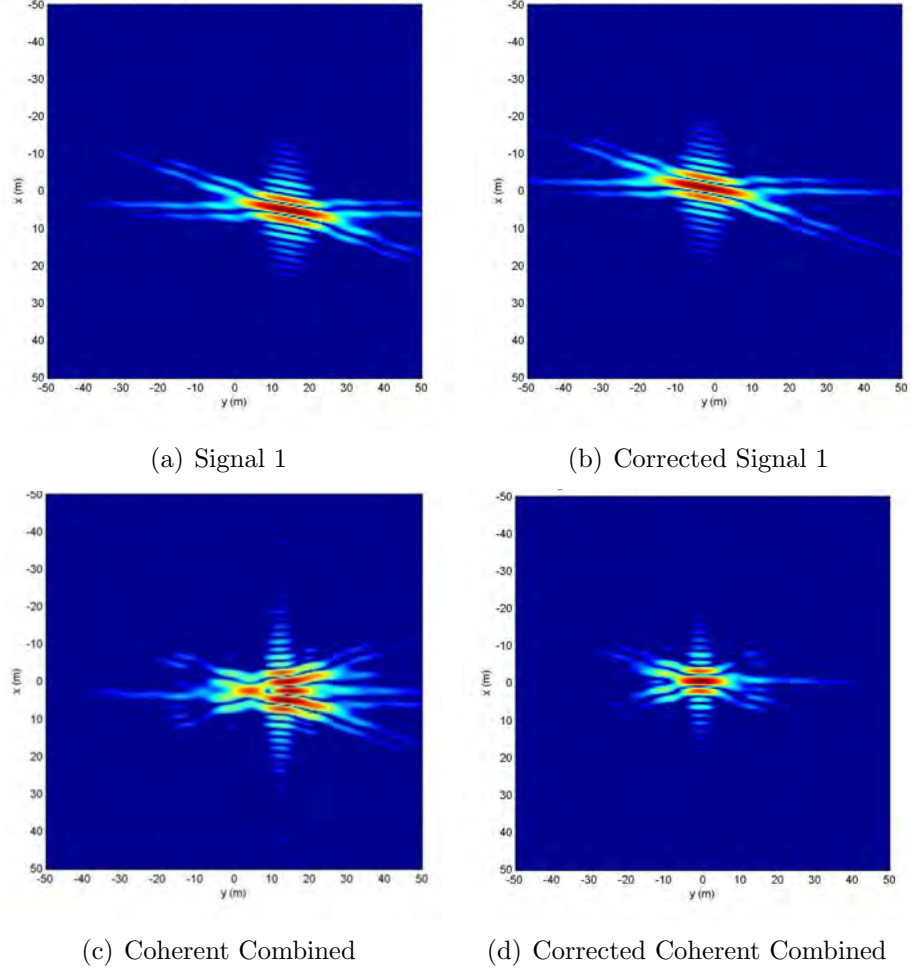


Figure 4.17. SAR images with linear error before and after correction

the inverse filtering random error correction is applied. The error applied is a random error function with a maximum and minimum range error of 7 m and -9 m respectively. The random error produces artifacts along the cross range dimension of the image. The inverse filtering technique is able to focus the image and show the target at the scene center.

Other observations included the moving of the target in range with a constant range error. The effects within the images are consistent with those seen in the literature. That is, quadratic error leads to a smearing in the cross range and a linear error leads to the moving of the target in cross range [16, 26]. The corrected

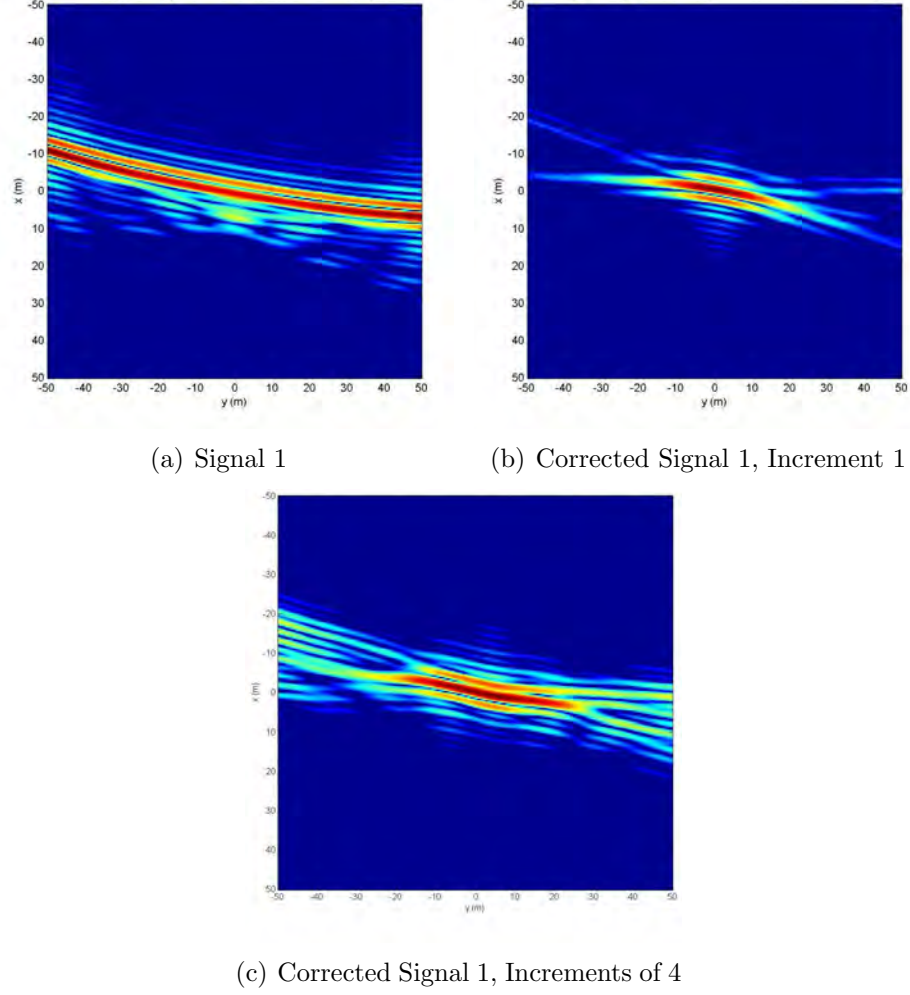


Figure 4.18. SAR images of Signal 1 with quadratic error before and after correction

images shown in this section demonstrate the inverse filtering technique is a useful method for focusing the images and correcting for the error in range. The size of increments determines the quality of the image correction, as expected. However, this technique is sufficient for a single, isolated point target, which makes it ideal for this research assumption. The most significant limitation is the assumption that some knowledge of the range error is known, or can be determined, from the single point target phase history data so as to estimate the error for phase correction in the processing.

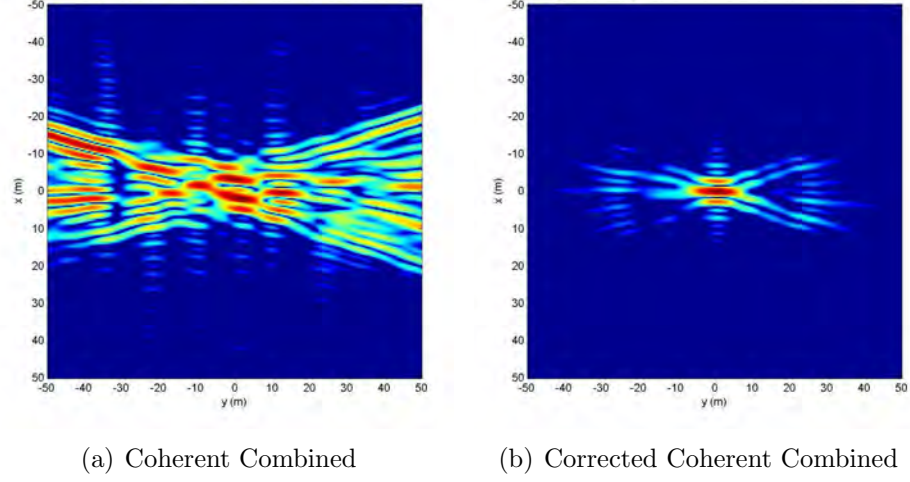


Figure 4.19. SAR images of coherent combined with random error before and after correction

4.4 Experimental Images

Five different data collections were taken using the experimental set up. The results of four collections are discussed and analyzed in this section. The results of the fifth collection do not provide any added value to the analysis. Table 4.4 details the parameters associated with the four data collections.

Table 4.4. Collection parameters, data collects 1-4

		Collect 1	Collect 2	Collect 3	Collect 4
Tx ₁	f_c (GHz)	2	2	2.2	2
	Θ (°)	35	35	25	25
Tx ₂	f_c (GHz)	2.5	2.5	2.5	2.5
	Θ (°)	-25	-35	-25	25
Rx	Aperture (°)	-20:2:20	-30:3:30	-20:2:20	-20:2:20
	Total Effective Aspect Aperture (°)	50	65	45	45

Each signal had a bandwidth of 200 MHz, receiver range set at 1.1 m, and all transmitter ranges were set at 0.25 m. The total effective aspect aperture represents

the angular aspect of the collection aperture when considering both angles of the transmitters and the receive aperture.

4.4.1 Data Collect 1.

The images created from the first data collection are shown in Figures 4.20 and 4.21 using the first and second signal processing methods respectively.

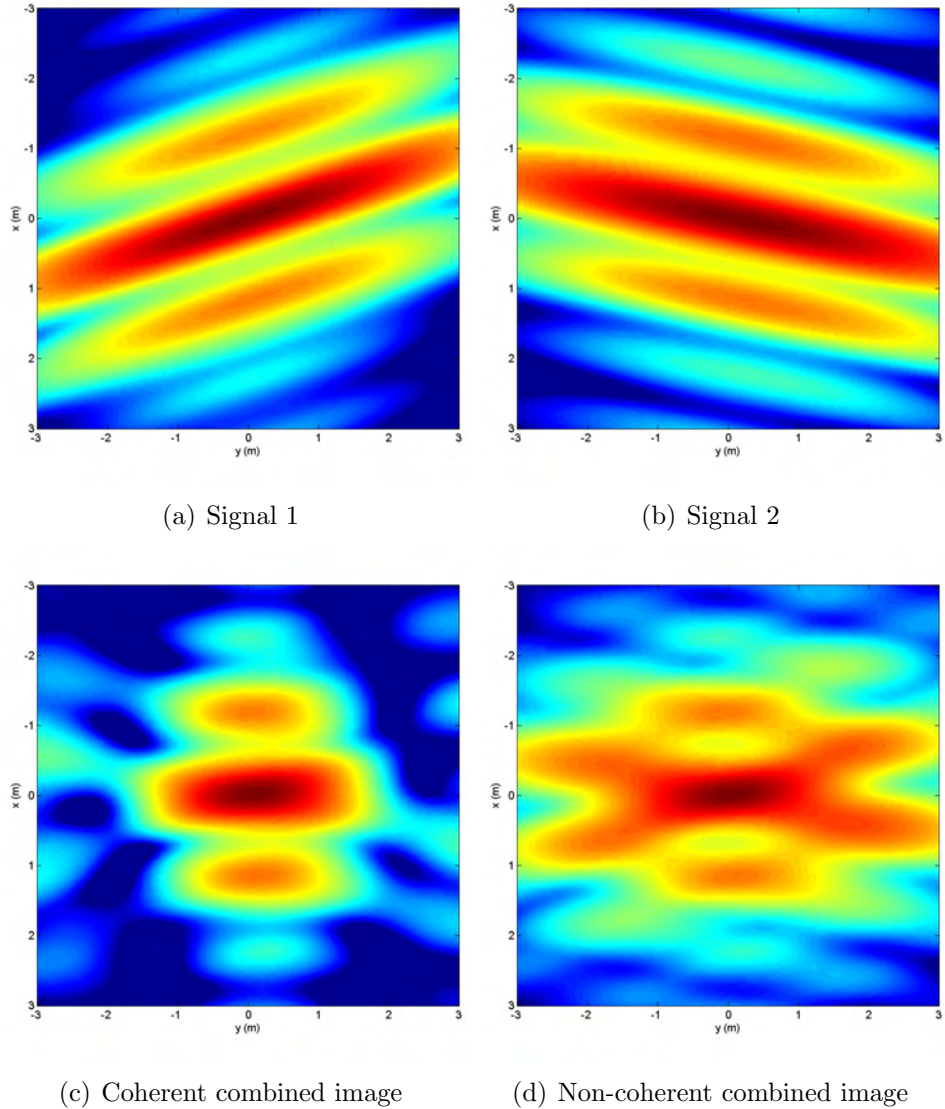


Figure 4.20. SAR images from data collect 1 using the signal separation and parallel processing method

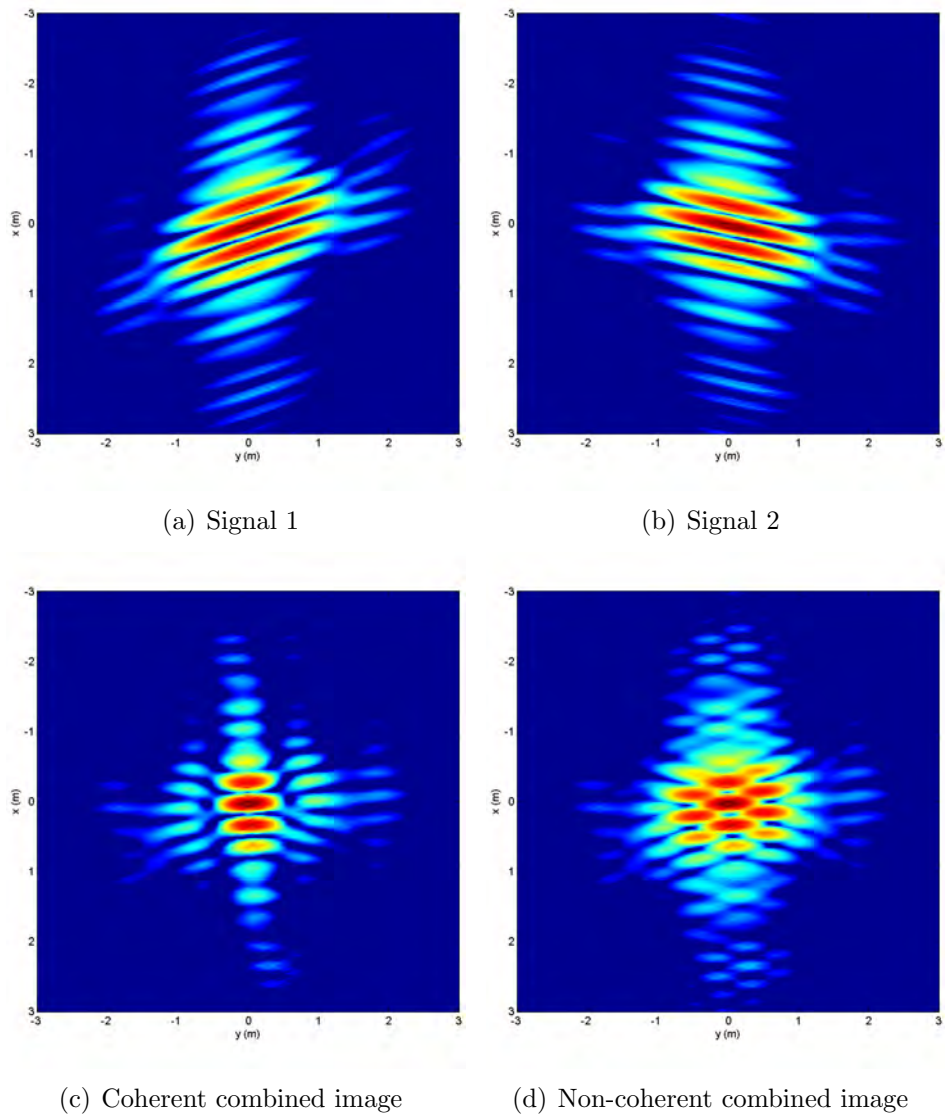


Figure 4.21. SAR images from data collect 1 using the combined reference signal processing method

Each of the four images generated using the FBP algorithm are shown, and the results are consistent with the simulation. Each of the individual signal images are oriented toward the respective bisector. Compared to the individual images, the coherent combined image shows a narrow target response at the scene center. The non-coherent image shows a heightened intensity around the target resulting from the constructive interference of sidelobe and main beam intensities.

The cross range resolution in the individual signal images along the range contour is measured to be 3.9 m. When the two images are combined, the measured resolution is 1.7 m, an improvement by a factor of 2.2. This is the result of the total effective aperture being more than twice the width of a single bistatic aperture

The images created using the second signal processing method are consistent with the observations of those in Figure 4.20, with the exception of the larger bandwidth, and hence finer range resolution.

Using a 200 MHz signal, with carrier separation of 500 MHz, results in a bandwidth extent of approximately 735 MHz (accounting for the slight increase as per the WiMAX standard). This leads a theoretical resolution of approximately 20 cm. The measured resolution in the image is approximately 16 cm, or a factor of 3.4 times finer than using the single 200 MHz signal. The sidelobe level is at -1.1 dB. These measured results are consistent with those found in the simulated data images.

4.4.2 Data Collect 2.

The images created from the second data collection are shown in Figures 4.22 and 4.23. This data collect provides a greater receiver collection aperture and a greater Θ_2 than the first data collect, and results in an increase in total aperture by 30%. The measured improvement in cross range resolution is calculated to be approximately 25%. Again, the second signal processing method shows a significant improvement over the single signal method in range resolution, but with the trade-off of much higher sidelobes. The geometric improvement from combining the images from signal 1 and signal 2 is consistent using both of the signal processing methods. Using the first method, the cross range resolution in the individual signals along the range contour is measured to be approximately 2.9 m. When the two images are combined, the measured resolution is 1.43 m, an improvement of slightly more than

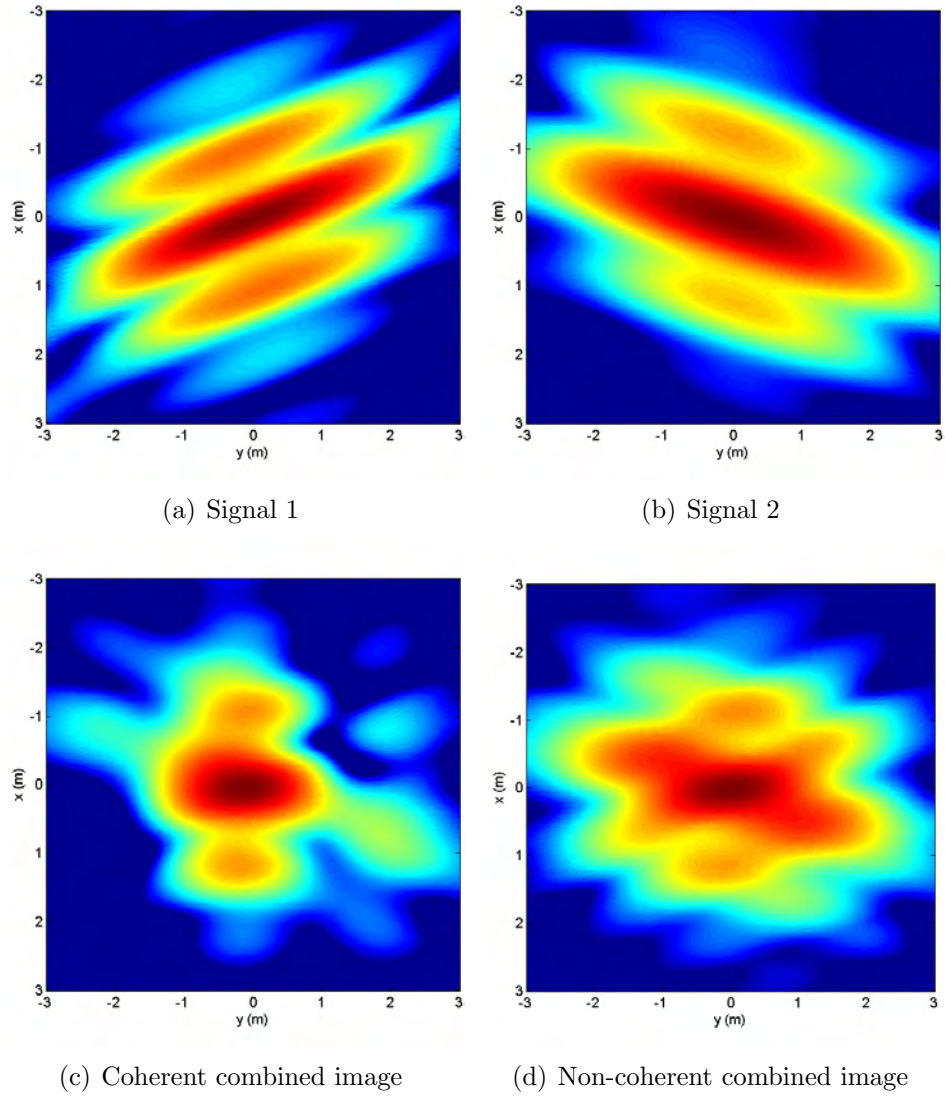


Figure 4.22. SAR images from data collect 2 using the signal separation and parallel processing method

half. This is expected given the total effective aperture of 65° is more than twice the width of a single bistatic aperture, which spans a total of 30° in this collection configuration.

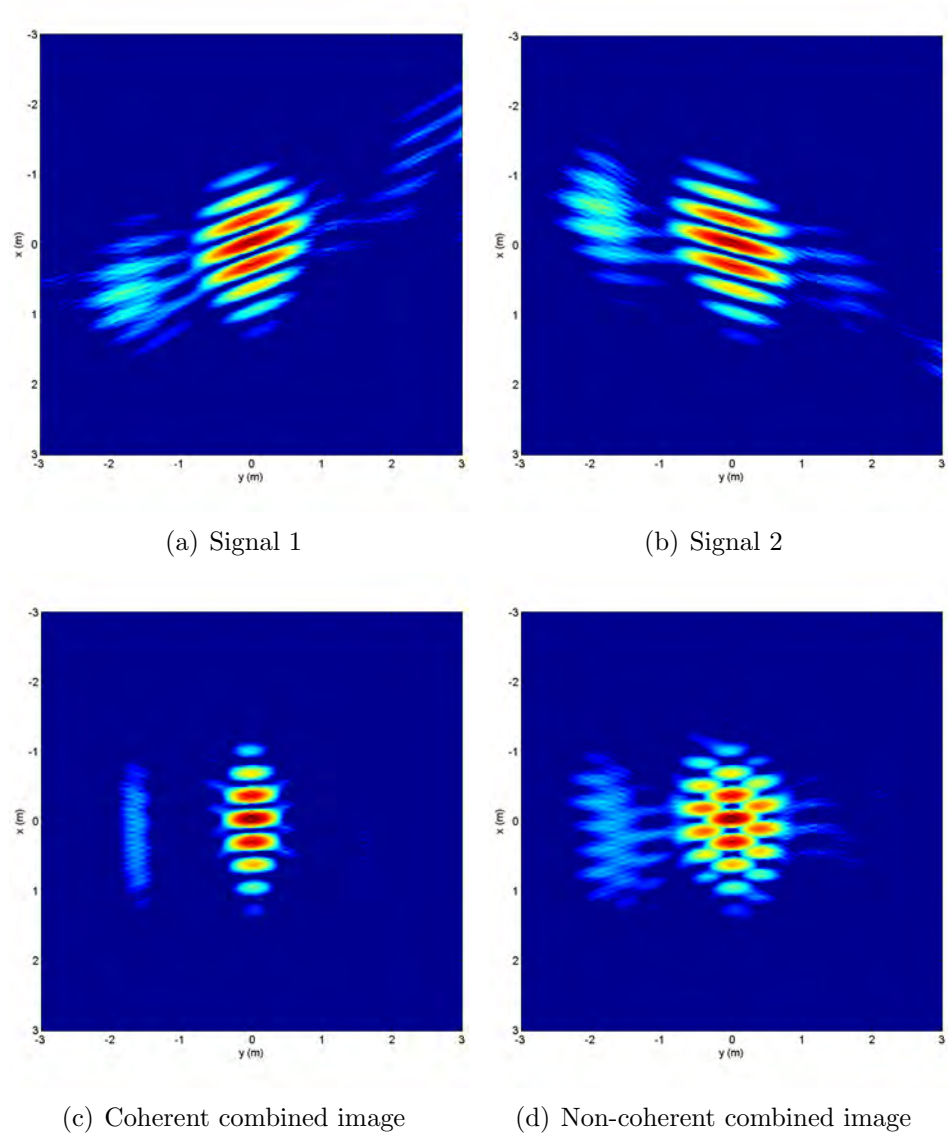


Figure 4.23. SAR images from data collect 2 using the combined reference signal processing method

4.4.3 Data Collect 3.

The final set of images were created from the third data collection and are shown in Figures 4.24 and 4.25. When compared to data collect 2, the receive collection aperture covers a smaller extent. Using data collect 3 as the baseline, the total effective aperture of collect 2 is 1.4 times wider, or 40% larger. The measured cross range resolution of data collect 3 is 2.4 m. The measured resolution within the images

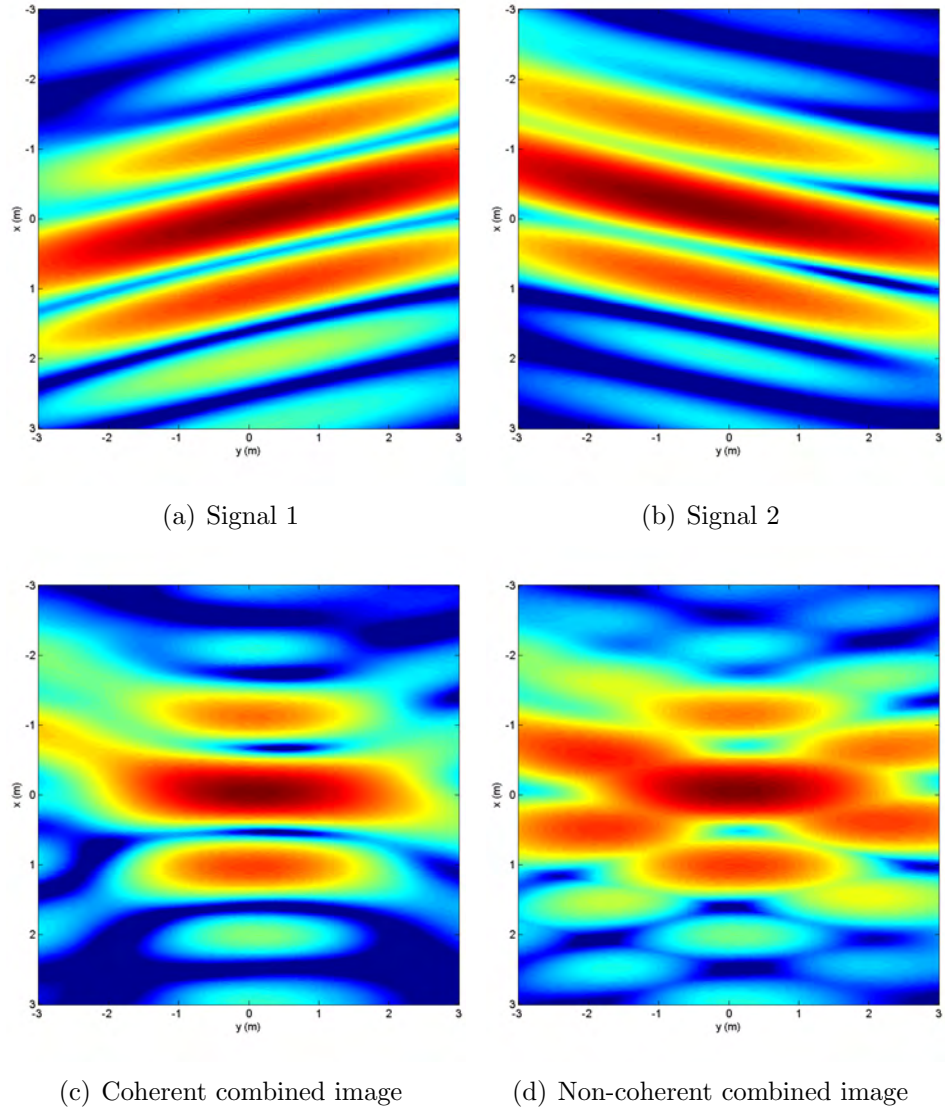


Figure 4.24. SAR images from data collect 3 using the signal separation and parallel processing method

of collect 2 is 1.43 m. This corresponds to an approximately 40% improvement on 2.4 m.

Using the first method, the cross range resolution in the individual signals is measured to be approximately 5 m. When the two images are combined, the measured resolution is 2.4 m, an improvement of more than half. Again, this is the result of the total effective aperture of 45° being more than twice the width of the individual

bistatic aperture, which spans a total of 20° in this collection configuration.

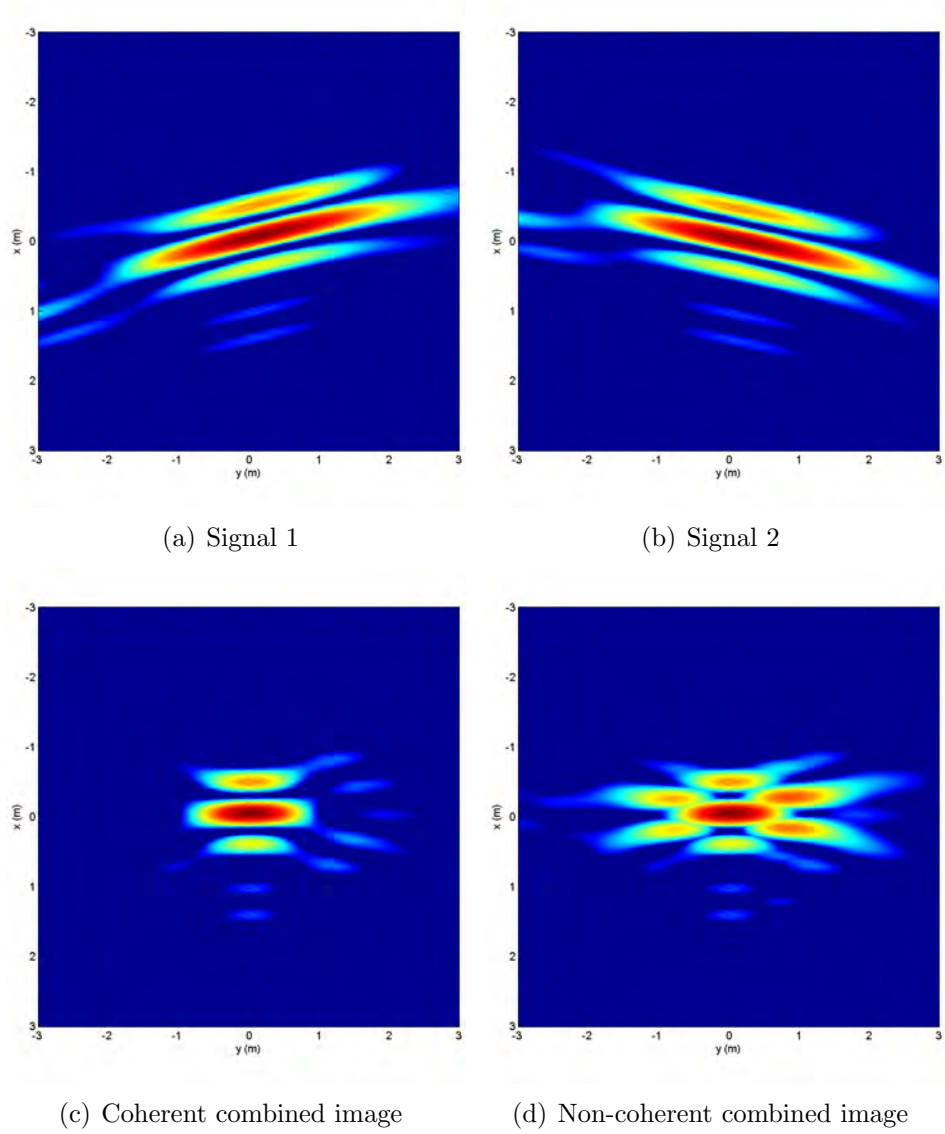


Figure 4.25. SAR images from data collect 3 using the combined reference signal processing method

4.4.4 Experimental Data Image Measurements.

Throughout all data collects, a signal bandwidth of 200 MHz was used. This bandwidth provides a resolution of 0.75 m, but using the WiMAX sampling rate, the actual range resolution is given by 0.65 m. In all images using the first method, the range resolution of the coherent combined images was measured to be $0.61 \text{ m} \pm 7 \text{ cm}$ (mean \pm st. dev.).

Using the second method, the range resolution was measured to be $0.16 \text{ m} \pm 0.6 \text{ cm}$ for a separation of 500 MHz. The theoretical value using these signals is 0.2 m. The sidelobe levels in the image using the second method were measured to be $-0.88 \text{ dB} \pm 0.23 \text{ dB}$. This is expected as the signal carrier separation is greater than the largest value used in the increment analysis in Section 4.2.5. However, for a separation of 300 MHz, as in data collect 3, the maximum sidelobe level was measured to be -3.8 dB, and the resolution is 24 cm. Both of these values are an improvement on the value given in Table 4.3. Increment 2 corresponds to a separation of 300 MHz using a 200 MHz bandwidth.

Table 4.5 lists the measured values from images generated from the experimental data collection.

Table 4.5. Measured values of range resolution and sidelobe level in experimental data images

	Method 1 Res (m)	Method 2 Res (m)	Method 2 SL level (dB)
Collect 1	0.6	0.16	-1.1
Collect 2	0.72	0.15	-0.9
Collect 3	0.55	0.24	-3.8
Collect 4	0.58	0.16	-0.65

4.4.5 Alternate Reference Signal.

The effect of an incorrect reference signal was analyzed using experimental data from collect 4. The experimental data was collected as per the test procedure in Section 3.7.2, however, the reference signals collected did not correspond to the distance of 1.35 m. This distance is the total path length relative to the scene center. Two different sets of reference signals were collected. The first was collected with an antenna separation of 0.35 m, therefore introducing a constant error of 1 m, or 0.5 m for each transmit and receive component. The second was collected directly from the AWG, therefore removing the cable lengths between the devices and the antennas and introducing a total error of 12.5 m, or constant error of 6.25 m each for the transmit and receive chain.

The images created using the constant error in the reference signal are shown in Figure 4.26 (a) and (c). With a constant error applied across the aperture, it is expected that the target will be shifted in the image in the range dimension, which is evident in this case. The measured shift in the two images are 0.6 m and 7.8 m respectively, which do not correlate to the exact distance expected (0.5 m and 6.25 m), but do illustrate a trend in using an inaccurate reference signal.

Figure 4.26 (b) and (d) show the corrected images generated using the FBP algorithm with the inverse filtering technique applied. The target range error measured in the image is doubled, to account for the total error, and this value is used as the range error within the inverse filtering phase correction function.

4.4.6 Comparison to Simulated Data.

Simulated phase history data was created using the same parameters in the experimental data collection, and images were created using the same FBP algorithm. Only the coherent combined images are presented in this thesis as means for comparison

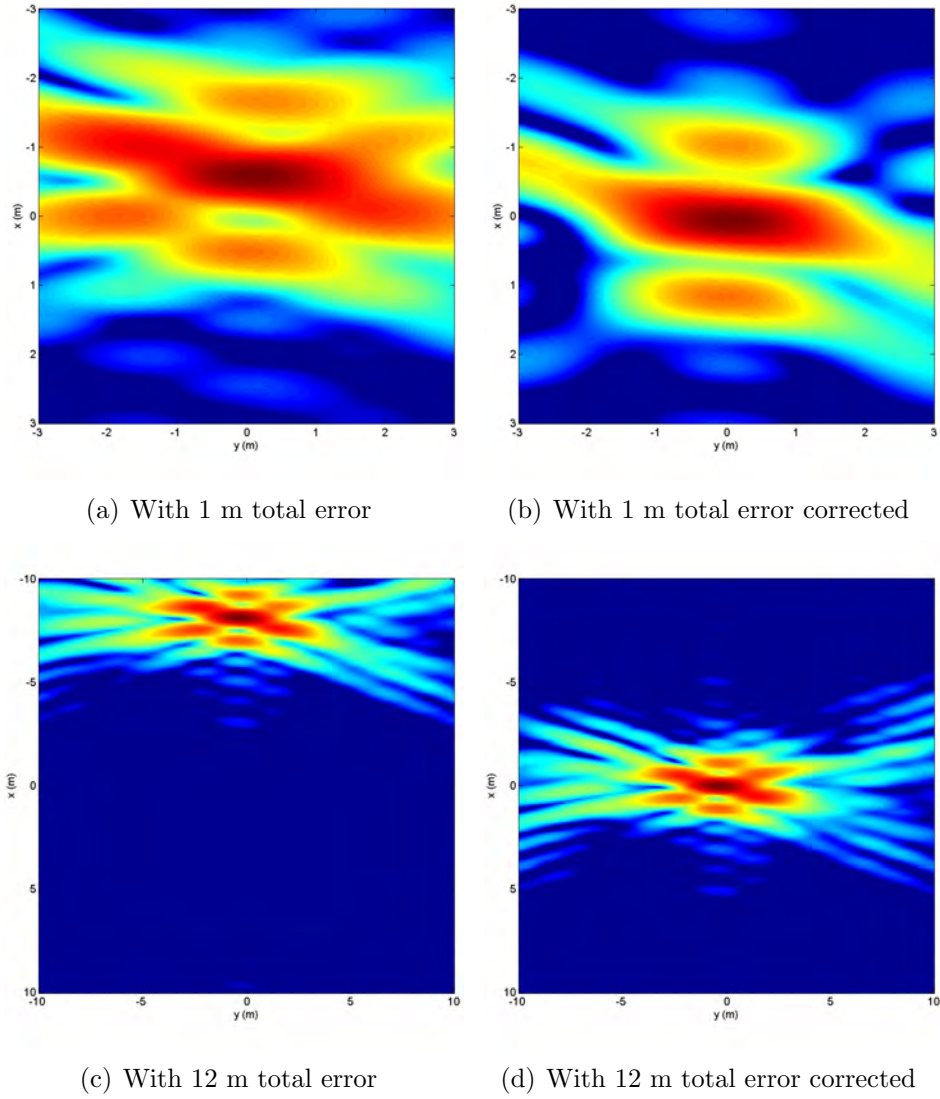


Figure 4.26. SAR images from data collect 4 using the signal separation and processing method with inaccurate reference signals

as the other three image types do not add any additional information. Figures 4.27 through 4.29 show three image comparisons, one for each data collect configuration.

Figure 4.27 shows a comparison between the coherent combined image using the signal separation method for data collect 1. The experimental data is found to have a better cross range resolution by a factor of 20%, however, the image does possess higher level artifacts and smearing around the target.

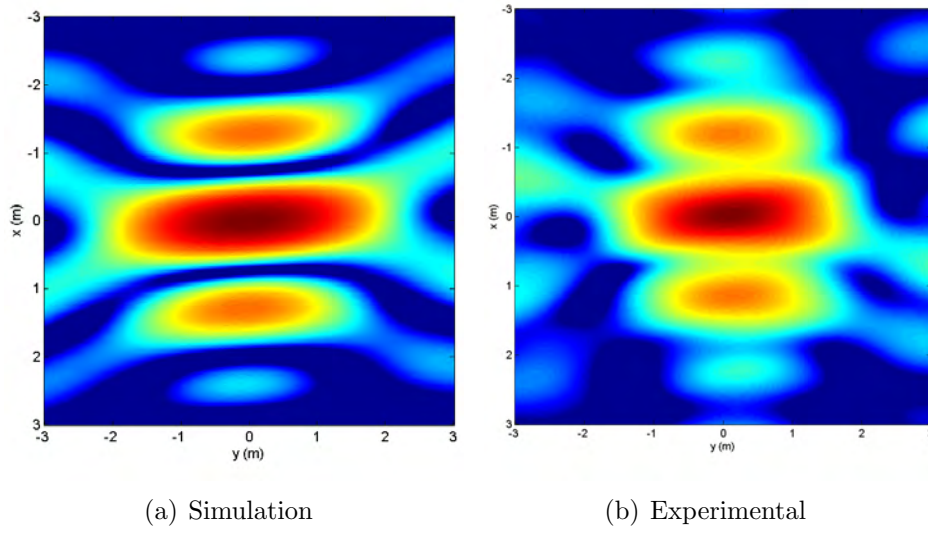


Figure 4.27. SAR images Simulated vs Experimental Data collect 1 using signal separation method

Figure 4.28 shows a comparison between the coherent combined image using the combined reference signal. The two images are very similar, again the experimental image does possess some minor artifacts off of the target location. Narrow range and cross range resolution are consistent through both images resulting from the increase in bandwidth and geometric diversity. The range resolution of the two images is measured to be 0.15 m, however the sidelobe level of the experimental data image is -0.9 dB compared to -1.55 dB in the simulated data image.

Figure 4.29 shows a comparison between the coherent combined image created with the combined reference signal method using the configuration of data collect 3. Again, similar characteristics are observed, with some very minor artifacts present in the cross range dimension for the experimental data. The range resolution in the experimental image is 0.24 m compared to 0.27 m in the simulation, and the sidelobe level is 0.5 dB lower than in the simulated data image.

A consistent observation in the experimental image when compared to the simulated data image is the presence of artifacts in the cross range dimension, albeit

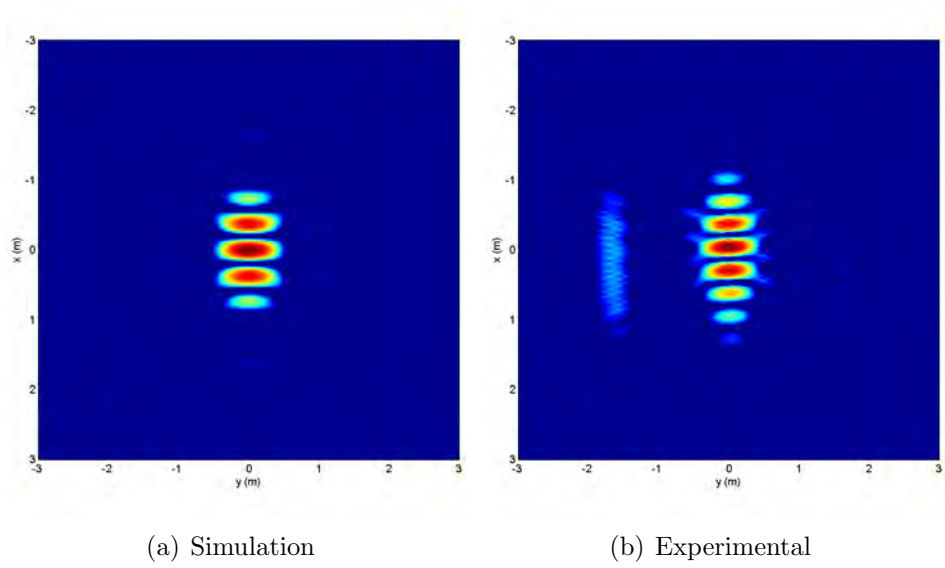


Figure 4.28. SAR images Simulated vs Experimental Data collect 2 using signal separation method

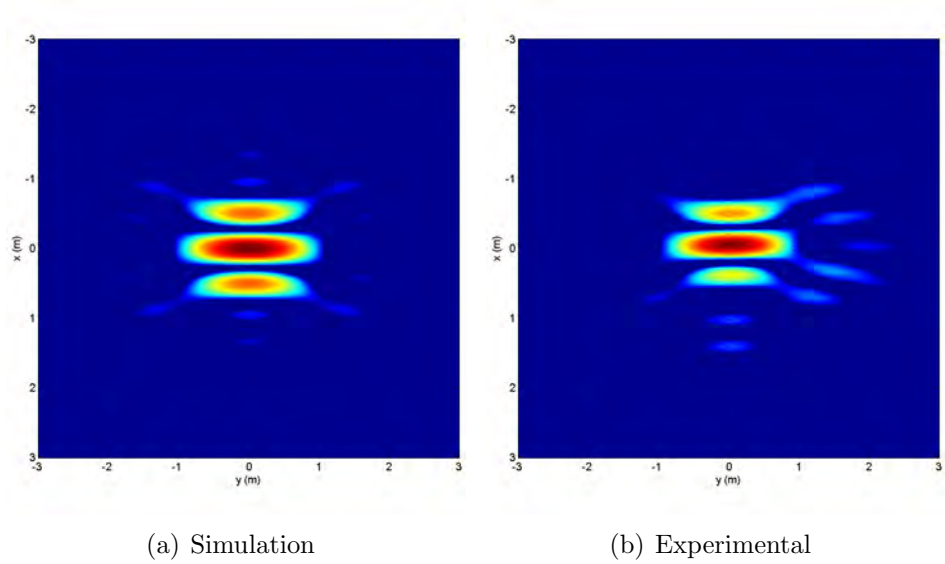


Figure 4.29. SAR images Simulated vs Experimental Data collect 3 using signal separation method

trivial. Artifacts in the cross range dimension may be attributed to some very minor random phase errors in the phase history data, but in this case the error is not large enough to influence the identification of the target. The experimental images do possess marginally better characteristics when compared to the simulated data images,

both in range and cross range resolution. In all cases, the experimental images are a true reflection of the simulated data images, and there are no significant discrepancies identified.

4.5 Summary of Findings and Observations

Simulated SAR images were generated for both the software and experimental data collections. For both signal processing methods, the observations in range and cross range resolution were consistent with those expected. A larger signal bandwidth improves the range resolution, while an increase in the aperture resulted in a finer cross range resolution. The combined reference signal approach was found to increase the range resolution of the target through the narrowing of the main lobe as expected, however, there exists the tradeoff with sidelobe level resulting from the properties of the Fourier transform and rectangular function separation. The experimental data images were found to be the similar to the simulated images, providing validation of the proposed proof of concept model.

The coherent combined image in all cases was found to have a finer resolution in cross range resolution than each of the individual images. This results from an increased total effective aperture determined by the geometric diversity in the two signal locations. If the two transmitter locations provided no angular diversity from one another, and therefore provide no improvement in the effective aperture, there would be no improvement in the combined image.

The inverse filtering approach was successfully applied to both the software simulated and experimental data to correct for errors in the image, and under the assumptions that some knowledge of the error in range is known and that the type of target is a single delta function.

4.6 Chapter Conclusion

The results and findings presented in this chapter demonstrate the foundation for multistatic radar imaging using the WiMAX signal. Simulated SAR images were created using a software model, consisting of two different approaches, and various parameters associated with the images analyzed. The observations were consistent with those expected. Additionally, images were created using an experimental data collection. The images created from the experimental collection displayed characteristics similar to both the expectations and the simulated data images. The next chapter will review the research objectives and underline conclusions based on the results detailed in this chapter.

V. Conclusions

5.1 Chapter Overview

Signals of opportunity such as commercial OFDM-based WiMAX waveforms have the potential to be used for passive radar imaging applications. The use of WiMAX signals for synthetic aperture radar applications is a particular stream of research at AFIT. This research effort was focused on demonstrating a proof-of-concept in using WiMAX signals to generate SAR images within a passive multistatic radar configuration. This chapter reviews the research goals, presents a summary of the research results and contributions, and outlines potential areas for future work in studying and developing the WiMAX signal for SAR applications.

5.2 Research Goals

To exploit signals of opportunity for radar applications, initial feasibility studies must be conducted into the selected waveform. This research effort investigated the feasibility of using the WiMAX waveform for use in SAR imaging, through the derivation of a mathematical model. This model was then developed in software to produce simulated SAR images using the filtered backprojection algorithm. To validate the model, an experiment within AFIT's Radar Instrumentation Laboratory was conducted and SAR images were produced using the same processing and imaging algorithms. This research provides a foundation for passive radar imaging research that can be further studied at AFIT.

5.3 Results and Contributions

The research effort successfully achieved the three primary research objectives. Based on the mathematical derivations, a software algorithm was developed which

generated phase history data using a matched filter process. This algorithm consisted of two signal processing approaches - signal separation and combined reference signals. Using this simulated phase history, SAR images of a point target were created using a modified FBP imaging algorithm. The image-based measured resolution characteristics of the target were consistent with the expectations.

Following simulations, experimental data collections were achieved using the AFIT developed experimental OFDM radar. The data collections were then processed using the same methods developed in the software model to produce simulated SAR images of the single target. The target behavior in the images was consistent with both expectations and results observed in the software model simulated data images.

The images created have successfully demonstrated proof-of-concept in using WiMAX signals to create SAR images of a target scene.

5.4 Future Work

Despite the achievement of all research objectives, there remains numerous areas for future study in the use of the WiMAX signal within a realistic SAR environment. Suggestions for future research concepts are presented in this section.

5.4.1 Research Scope.

The scope of this research was limited by numerous assumptions to generate phase history data. Some of these assumptions are not realistic when considering the real-world environment in which passive SAR imaging is conducted. Future work in this area may include disregarding some assumptions, such as:

- Removing frequency orthogonality such that there is now overlap in the spectral response of the two signals. Investigate the effects of spectral overlap with the proposed models.

- Altering the PRF or the transmit time of the two transmit signals such that they do not transmit simultaneously.
- Investigating the results of numerous targets of different geometric parameters, such as a plate or trihedral.

5.4.2 Software Model.

The software model used within this research was developed under the basis of the assumptions. If some of the assumptions were relaxed, then the model could be extended to include and simulate the revised scope. Some of the revisions include:

- Using targets with different geometric properties which will alter the phase characteristics of the return signal. The current model assumes point targets, with a reflectivity function of a delta function.
- Improving the model to account for transmitter angles of $\Theta > 90^\circ$. The current model allows bistatic angles from the aperture center to the transmitter of less than 90° , so the transmitters lie within the azimuthal range of $\Theta \in [-90 : 90^\circ]$.

5.4.3 Experimental Data Collection.

The experimental data collection was conducted within the confined space of RAIL for a single target. An experimental data collection could be conducted using a much larger space with numerous targets at different ranges. This collection could occur outside, with multiple targets at greater ranges both on and off the scene center. The robustness of the proposed model could be tested using this experimental data collection.

Bibliography

- [1] “IEEE Standard for Local and Metropolitan Area Networks Part 16: Air Interface for Fixed Broadband Wireless Access Systems”, 2004.
- [2] Berger, C. R. and J. M. F. Moura. “Noncoherent Compressive Sensing With Application to Distributed Radar”. *Information Sciences and Systems (CISS), 2011 45th Annual Conference on*, 1–6. 2011.
- [3] Bongioanni, C., F. Colone, and P. Lombardo. “Performance Analysis of a Multi-frequency FM based Passive Bistatic Radar”. *Radar Conference, 2008. RADAR '08. IEEE*, 1–6. 2008.
- [4] Burns, A. J. “Chip Rate Passive Radar Journal”, 2008. URL {<http://chiprate.co.uk>}.
- [5] Chernyak, V. S. *Fundamentals of Multisite Radar Systems*. Gordon and Breach Science Publishers, 1998.
- [6] Falcone, P., F. Colone, C. Bongioanni, and P. Lombardo. “Experimental Results for OFDM WiFi-based Passive Bistatic Radar”. *Radar Conference, 2010 IEEE*, 516–521. 2010.
- [7] Griffiths, H. “Multistatic, MIMO and Networked Radar: The Future of Radar Sensors?” *Radar Conference (EuRAD), 2010 European*, 81–84. 2010.
- [8] Griffiths, H. and C. Baker. “The Signal and Interference Environment in Passive Bistatic Radar”. *Information, Decision and Control, 2007. IDC '07*, 1–10. 2007.
- [9] Griffiths, H. D. “New Directions in Bistatic Radar”. *Radar Conference, 2008. RADAR '08. IEEE*, 1–6. 2008.
- [10] Griffiths, H. D. and C. J. Baker. “Measurement and Analysis of Ambiguity Functions of Passive Radar Transmissions”. *Radar Conference, 2005 IEEE International*, 321–325. 2005.
- [11] Griffiths, H. D. and C. J. Baker. “Passive Coherent Location Radar Systems. Part 1: Performance Prediction”. *Radar, Sonar and Navigation, IEE Proceedings* -, 152(3):153–159, 2005.
- [12] Gutierrez del Arroyo, J. R. and J. A. Jackson. “Range Profiles from an Experimental OFDM Passive Radar”. *Waveform Design and Diversity Conference*. 22-27 January 2012.
- [13] Gutierrez del Arroyo, J. R. and J. A. Jackson. “SAR Imaging Using WiMAX OFDM PHY”. *Radar Conference (RADAR), 2011 IEEE*, 129–134. 2011.

- [14] Gutierrez del Arroyo, J. R., J.A. Jackson, and M. Temple. “WiMAX Ambiguity Function for PCL systems”. *Aerospace and Electronics Conference (NAECON), Proceedings of the IEEE 2010 National*, 54–59. 2010.
- [15] Jain, A. K. *Fundamentals of Digital Image Processing*. Prentice Hall, Inc., Upper Saddle River, NJ, 1986.
- [16] Jakowatz Jr, C.J., D. E. Wahl, P. H. Eichel, D. C. Ghiglia, and P. A. Thompson. *Spotlight-Mode Synthetic Aperture Radar: A Signal Processing Approach*. Springer Science + Business Media, Inc., New York, NY, 1996.
- [17] Kulpa, Krzysztof. *Continuous Wave Radars, Monostatic, Multistatic and Network*, volume 2 of *Advances in Sensing with Security Applications*, 215–242. Springer Netherlands, 2006.
- [18] Lauri, A., F. Colone, R. Cardinali, C. Bongioanni, and P. Lombardo. “Analysis and Emulation of FM Radio Signals for Passive Radar”. *Aerospace Conference, 2007 IEEE*, 1–10. 2007.
- [19] Nies, H., O. Loffeld, K. Natroshvili, and A. M. Ortiz. “A Solution for Bistatic Motion Compensation”. *Geoscience and Remote Sensing Symposium, 2006. IGARSS 2006. IEEE International Conference on*, 1204–1207. 2006.
- [20] O’Hagan, D. W., F. Colone, C. J. Baker, and H. D. Griffiths. “Passive Bistatic Radar (PBR) demonstrator”. *Radar Systems, 2007 IET International Conference on*, 1–5. 2007.
- [21] Richards, M. A., J. A. Scheer, and W. A. Holm. *Principles of Modern Radar*. Scitech Publishing, Rayleigh, NC, 2010.
- [22] Skolnik, M. I. *Radar Handbook*. The McGraw-Hill Companies, third edition, 2008.
- [23] Soumekh, M. *Synthetic Aperture Radar Signal Processing with MATLAB Algorithms*. John Wiley & Sons, Inc, Canada, 1999.
- [24] Sullivan, R.J. *Radar Foundations for Imaging and Advanced Concepts*. SciTech Publishing Inc, 2004.
- [25] Willis, N. J. *Bistatic Radar*. Artech House, 1991.
- [26] Willis, N. J. and H. D. Griffiths. *Advances in Bistatic Radar*. Scitech Publishing, Raleigh, NC, 2007.
- [27] Yarman, C. E. and B. Yazici. “Synthetic Aperture Hitchhiker Imaging”. *Image Processing, IEEE Transactions on*, 17(11):2156–2173, 2008.

REPORT DOCUMENTATION PAGE

Form Approved
OMB No. 0704-0188

The public reporting burden for this collection of information is estimated to average 1 hour per response, including the time for reviewing instructions, searching existing data sources, gathering and maintaining the data needed, and completing and reviewing the collection of information. Send comments regarding this burden estimate or any other aspect of this collection of information, including suggestions for reducing this burden to Department of Defense, Washington Headquarters Services, Directorate for Information Operations and Reports (0704-0188), 1215 Jefferson Davis Highway, Suite 1204, Arlington, VA 22202-4302. Respondents should be aware that notwithstanding any other provision of law, no person shall be subject to any penalty for failing to comply with a collection of information if it does not display a currently valid OMB control number. **PLEASE DO NOT RETURN YOUR FORM TO THE ABOVE ADDRESS.**

1. REPORT DATE (DD-MM-YYYY) 22-03-2012			2. REPORT TYPE Master's Thesis		3. DATES COVERED (From — To) Aug 2010 — Mar 2012	
4. TITLE AND SUBTITLE Passive Multistatic Radar Imaging using an OFDM based Signal of Opportunity					5a. CONTRACT NUMBER	
					5b. GRANT NUMBER	
					5c. PROGRAM ELEMENT NUMBER	
6. AUTHOR(S) Rapson, Matthew, B.P., FLTLT, RAAF					5d. PROJECT NUMBER	
					5e. TASK NUMBER	
					5f. WORK UNIT NUMBER	
7. PERFORMING ORGANIZATION NAME(S) AND ADDRESS(ES) Air Force Institute of Technology Graduate School of Engineering and Management (AFIT/EN) 2950 Hobson Way WPAFB OH 45433-7765					8. PERFORMING ORGANIZATION REPORT NUMBER AFIT/GE/ENG/12-35	
9. SPONSORING / MONITORING AGENCY NAME(S) AND ADDRESS(ES) Dr Alan Kerrick Air Force Research Laboratory 2241 Avionics Drive Area B B620 WPAFB OH 45433 (937) 735-6427 x4332; alan.kerrick@wpafb.af.mil					10. SPONSOR/MONITOR'S ACRONYM(S) AFRL	
					11. SPONSOR/MONITOR'S REPORT NUMBER(S)	
12. DISTRIBUTION / AVAILABILITY STATEMENT APPROVED FOR PUBLIC RELEASE; DISTRIBUTION UNLIMITED.						
13. SUPPLEMENTARY NOTES This material is declared a work of the U.S. Government and is not subject to copyright protection in the United States.						
14. ABSTRACT This paper demonstrates a proof of concept in using an OFDM-based signal of opportunity for SAR imaging purposes within a passive, multistatic radar construct. Two signal processing methods have been proposed to create phase history data. The same methods are applied in both a simulated software model and an experimental data collection environment to produce simulated SAR images using the CBP imaging algorithm. The images generated from both the experimental and simulated data were observed to be consistent with each other and with expectations in terms of resolution. Coherent addition of the images results in improved image resolution due to the geometric and frequency diversity of the multistatic scenario compared to the individual bistatic pairs.						
15. SUBJECT TERMS Passive Radar, synthetic aperture radar (SAR), radar imaging, OFDM, WiMAX, Multistatic, filtered backprojection (FBP)						
16. SECURITY CLASSIFICATION OF:			17. LIMITATION OF ABSTRACT	18. NUMBER OF PAGES	19a. NAME OF RESPONSIBLE PERSON	
a. REPORT	b. ABSTRACT	c. THIS PAGE			Dr. Julie A. Jackson, PhD	
U	U	U	UU	106	19b. TELEPHONE NUMBER (include area code) (937) 255-3636 x4678; julie.jackson@afit.edu	